

Variability of Total Electron Content (TEC) during Four Major Geomagnetic Storms of 2012–2014: A Multisite Analysis at Fixed Longitudes

Abstract

This study investigates the ionospheric response to four major geomagnetic storms that occurred on 14 July 2012, 17 March 2013, 2 October 2013, and 27 February 2014, focusing on variations in the vertical total electron content (VTEC). VTEC data were obtained from 13 GNSS stations distributed across low, mid, and high-latitude regions along longitudes between 20°E and 40°E. For each event, the mean VTEC of the five geomagnetically quietest days of the corresponding month was used as a reference to characterize storm-time deviations. The results reveal diverse and complex ionospheric responses. The 14 July 2012 storm is characterized by a nighttime VTEC depletion at the equatorial ionization anomaly (EIA) trough, a transient intensification of the EIA, pronounced oscillations, interhemispheric asymmetries, and a subsequent suppression of the EIA, while high latitudes exhibit persistent depletion. The 17 March 2013 storm shows a pre-storm enhancement of VTEC, followed by oscillatory behavior, a transition from positive to negative storm effects, interhemispheric asymmetries, and EIA suppression. Similarly, the 2 October 2013 storm exhibits an early VTEC enhancement, marked oscillations, high-latitude depletion, and a transition from positive to negative effects at mid-latitudes, with relatively weak responses at low latitudes. In contrast, the 27 February 2014 storm is dominated by a widespread positive VTEC response, except at southern high latitudes where negative effects prevail, together with pronounced interhemispheric asymmetries. These findings highlight the strong spatiotemporal variability of storm-time ionospheric responses as a function of storm intensity, latitude, and likely the local time of main phase onset. The observed signatures are interpreted in terms of the combined effects of prompt penetration electric fields (PPEF), disturbed dynamo electric fields (DDEF), traveling atmospheric disturbances (TADs), and storm-induced changes in thermospheric composition, particularly variations in the O/N₂ ratio.

Copy Right, IJAR, 2019, All rights reserved.

1
2
3 **Introduction:-**
4 The ionosphere, extending from approximately 60 km to 1000 km in altitude, constitutes the ionized component of
5 Earth's upper atmosphere and plays a fundamental role in space weather processes through its coupling with the
6 magnetosphere and its sensitivity to solar and geomagnetic forcing (Pulkkinen 2007; Ouédraogo et al. 2024 ;
7 Alenazi et al. 2025). During geomagnetic storms, the ionosphere undergoes substantial perturbations, commonly
8 referred to as ionospheric storms, which significantly affect radio wave propagation and degrade the accuracy of
9 Global Navigation Satellite System (GNSS) positioning and navigation services (Davies 1990; Blanch et al. 2013;
10 Curto et al. 2018; Atıcı et Sağır 2020). A comprehensive understanding of storm-time ionospheric behavior is
11 therefore crucial for both scientific investigations and operational applications (Migoya-Orué et al. 2009; Liu et al.
12 2011; Akala et al. 2012).
13 The ionospheric response to geomagnetic storms depends on multiple factors, including storm intensity, local time,
14 season, geomagnetic latitude and longitude, storm phase, and the prevailing level of solar activity (Prölss 1995; Gao
15 2008; Mendillo et Narvaez 2009; Pedatella et al. 2009; Mendillo et Narvaez 2010; Vijaya Lekshmi et al. 2011;
16 Immel et Mannucci 2013; Matamba et al. 2015). Based on geomagnetic latitude (GLAT), the ionosphere is
17 commonly classified into low (GLAT < 30°), mid (30° ≤ GLAT < 60°), and high latitudes (GLAT ≥ 60°)
18 (Hunsucker et Hargreaves 2007). Geomagnetic storms are categorized using the Dst index as weak (-50 nT < Dst ≤
19 -30 nT), moderate (-100 nT < Dst ≤ -50 nT), and intense (Dst ≤ -100 nT) events (Gonzalez et al. 1994).

20 Among the parameters used to monitor ionospheric disturbances, the vertical total electron content (VTEC) is one of
21 the most sensitive indicators. Storm-time VTEC variability is controlled by several physical mechanisms, including
22 prompt penetration electric fields (PPEF), disturbed dynamo electric fields (DDEF), thermospheric composition
23 changes, and storm-induced neutral winds. The interplay of these processes can lead to either positive or negative
24 ionospheric storm effects, depending on geophysical conditions (Prölss 1995; Buonsanto 1999; Richmond et Lu
25 2000; Mendillo 2006; Balan et al. 2010).

26 Numerous studies have examined TEC variability during major geomagnetic storms of solar cycle 24, particularly
27 between 2012 and 2014. However, most investigations have focused on the American and Asian longitude sectors
28 (Qian, Solomon, et al. 2014; Chakraborty et al. 2015; Mao et al. 2015; Shreedevi et Choudhary 2017; Migoya-Orué
29 et al. 2021; Zhu et al. 2022). In contrast, studies in the Europe–Africa sector remain relatively sparse and
30 fragmented. Akala et al. (2013) investigated equatorial and mid-latitude responses in East Africa, while Azzouzi
31 (2016) analyzed storm-time ionospheric behavior at mid and high latitudes over the Europe–Africa region. More
32 localized studies using a limited number of GNSS stations were conducted by Malki et al. (2018) and Habyarimana
33 (2023). Tesema et al. (2015), although covering a relatively broad latitudinal range, did not include southern high
34 latitudes and focused primarily on VTEC map-based interpretations. Shimeis et al. (2015) analyzed TEC variations
35 along a latitudinal chain of GPS stations between 20°E and 40°E, spanning from northern to southern high latitudes,
36 but their study was limited to the 5 April 2010 storm. Global modeling and simulation studies (Yue et al. 2016) have
37 included the Europe–Africa sector; however, their emphasis remained predominantly on the American and Asian
38 sectors.

39 Despite providing valuable insights into the underlying physical mechanisms (PPEF, DDEF, neutral winds, and
40 thermospheric composition changes expressed through the O/N₂ ratio), these studies do not offer a comprehensive
41 and coherent regional analysis covering all latitudes along a fixed longitude sector.

42 In this context, the present study aims to analyze VTEC variability during four major geomagnetic storms of solar
43 cycle 24 using GNSS stations distributed along a Europe–Africa–Antarctic meridional chain between 20°E and
44 40°E. The methodology combines a station-by-station analysis, in which daily VTEC variations are compared with
45 the mean VTEC of the five quietest days of the corresponding month, with the analysis of regional VTEC and
46 Δ VTEC maps. This approach allows for a detailed characterization of both local and regional ionospheric responses
47 and provides new insight into the equatorial and interhemispheric dynamics associated with geomagnetic storms.

48 The paper is organized as follows: Section 2 describes the data and methodology, Section 3 presents and discusses
49 the results, and Section 4 provides the interpretation and main conclusions.

50

51 **1. Data and Methods**

52 **1.1. Data**

53 **1.1.1. Solar Wind and Geomagnetic Parameters**

54 In this study, we used several solar wind parameters, including the solar wind speed (V_{sw}, km s⁻¹), solar wind
55 dynamic pressure (P_{sw}, nPa), and the south–north component of the interplanetary magnetic field (IMF B_z, nT), as
56 well as geomagnetic indices such as the auroral electrojet index (AE, nT), the symmetric ring current index
57 (SYM/H, nT), the equatorial Dst index, and the planetary K_p index.

58 Time series of V_{sw}, P_{sw}, B_z, AE, and SYM/H were obtained from the OMNI database with a 1-minute temporal
59 resolution, available at the OMNIWeb portal (https://omniweb.gsfc.nasa.gov/form/omni_min.html). The K_p and Dst
60 indices, together with the storm sudden commencement (SSC) times marking the abrupt onset of geomagnetic
61 storms, were retrieved from the International Service of Geomagnetic Indices (ISGI) website
62 (https://isgi.unistra.fr/data_download.php).

63 The SYM/H index, which is closely related to the Dst index, provides a higher temporal resolution and allows for a
64 more detailed monitoring of ring current evolution and associated variations in Earth’s magnetic field. All these
65 parameters were used to identify isolated geomagnetic storms, quantify their intensity, and track their temporal
66 evolution (Gonzalez et al. 1994; Tsurutani et al. 1997; Kelley 2009).

67 **1.1.2. Ionospheric Parameter: VTEC**

68 The ionospheric response to the geomagnetic storms of 14 July 2012, 17 March 2013, 2 October 2013, and 27
69 February 2014 was analyzed using vertical total electron content (VTEC) data computed with software developed by
70 Fleury (MATLAB-based code, www.girgea.org). The analysis is based on observations from 13 GNSS stations
71 regularly distributed across low-, mid-, and high-latitude regions along a longitudinal sector between 20°E and 40°E.
72 RINEX observation files for the selected stations were downloaded from the UNAVCO data archive
73 (<http://www.unavco.org>). Figure 1 shows the geographical distribution of the GNSS stations used in this study,
74 together with the position of the magnetic equator, located near 10° N in geographic latitude. The magnetic equator
75 is an essential reference, as the equatorial ionization anomaly (EIA) is strongly controlled by the geomagnetic field
76 configuration. Table 1 lists the geographic and geomagnetic coordinates of all stations.

77 The ionospheric parameter considered in this study is the vertical total electron content (VTEC), which represents
78 the number of electrons contained in a vertical column of 1 m² cross-sectional area extending up to the satellite
79 altitude. The slant total electron content (STEC) was computed using the dual-frequency combination (f₁ = 1575.42
80 MHz and f₂ = 1227.60 MHz) of pseudorange measurements contained in the RINEX files, with a temporal
81 resolution of 30 s.

82 STEC values were calibrated by accounting for satellite differential code biases (DCBs) provided by the Center for
83 Orbit Determination in Europe (CODE) at the University of Bern. Receiver DCBs were estimated by fitting the
84 measured STEC to STEC values derived from the GIM/CODG model (<ftp://aiub.unibe.ch>). The DCB applied
85 corresponds to the daily mean value. A mapping function with a reference height of 450 km was then used to
86 convert STEC to VTEC (Ouédraogo et al. 2024; Ouattara et al. 2011):

$$VTEC = STEC \times \sqrt{1 - \left(\frac{R_T \cos^2 \theta}{R_T + h_{ref}} \right)^2}$$

87 where R_T is Earth's radius, θ is the satellite elevation angle, and h_{ref} denotes the reference height.
88 VTEC is expressed in total electron content units (TECU), where 1 TECU = 10¹⁶ electrons. m⁻². VTEC values are
89 assigned to the ionospheric pierce point (IPP) corresponding to each satellite. The vertical TEC above each station
90 was finally obtained through an inverse-square elevation-weighted regression applied to all satellite observations
91 within each time interval. The use of VTEC is particularly relevant, as it provides a direct indicator of the global
92 ionospheric state and enables an accurate characterization of ionospheric variability during geomagnetic storms.
93

94 **1.1.3. Thermospheric Composition Data**

95 In addition, global maps of the [O/N₂] ratio derived from the Global Ultraviolet Imager (GUVI) onboard the TIMED
96 satellite were used to support the interpretation of the results. These maps, available from the portal
97 https://guvitimed.jhuapl.edu/guvi-gallery1son2_new/, constitute a key indicator of the thermospheric state and of
98 electron density variations in the ionospheric F region (Yu et al. 2023).

99 A decrease in atomic oxygen reduces ion production, while an increase in molecular nitrogen enhances ion loss
100 through recombination processes, leading to a net decrease in electron density (Prölss 1995). Consequently, the
101 [O/N₂] ratio is particularly well suited for assessing ionospheric and thermospheric responses to geomagnetic storms
102 (Rishbeth et Müller-Wodarg 2006; Fuller-Rowell et al. 2007; Yue et al. 2014).

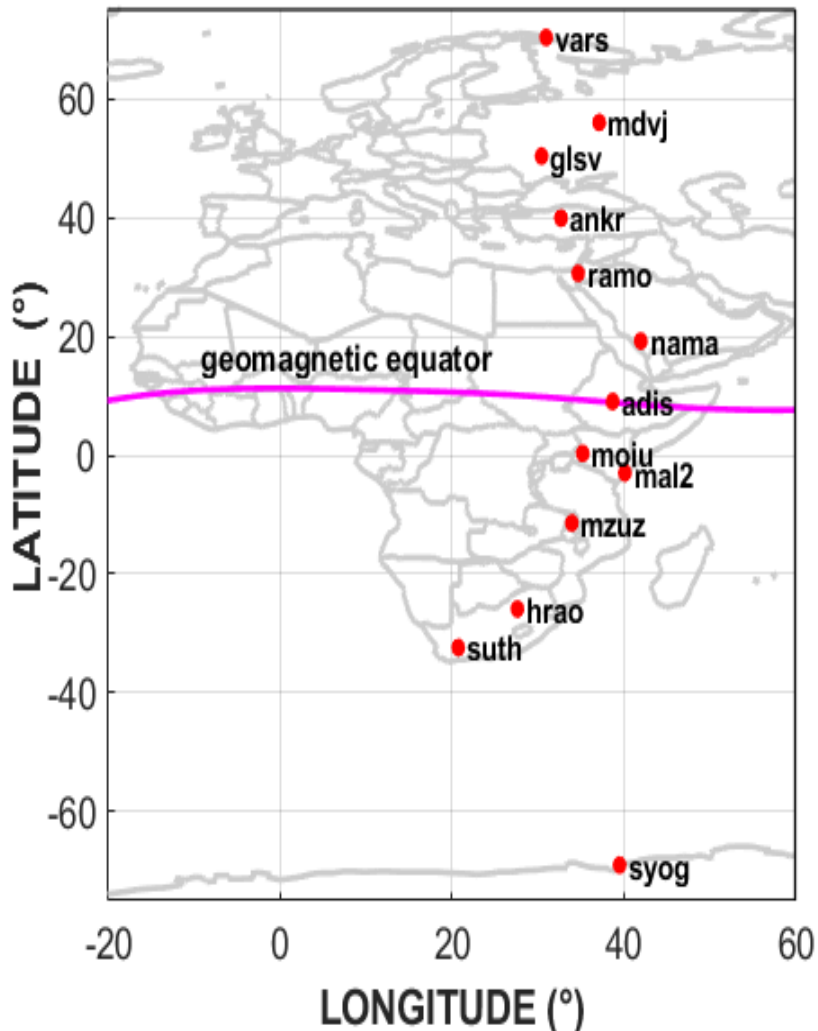


Figure 1: Map showing the location of the selected GNSS receivers

Table 1: GNSS stations and their geographic and geomagnetic coordinates.

Region	Station	Lat (°)	Lon (°)	Lat mag. (°)	Lon mag. (°)	Local Time
High latitude	VARS	70.33	31.03	66.50	113.32	UTC+2h
Mid-latitude	SVTL	60.53	29.78	56.61	106.79	UTC+2h
	GLSV	50.36	30.50	45.96	104.50	UTC+2h
	ANKR	39.89	32.76	34.24	04.97	UTC+2h
Low latitude	RAMO	30.60	34.76	23.36	106.26	UTC+2h
	NAMA	19.21	42.04	11.49	113.60	UTC+3h
	ADIS	9.03	38.76	0.16	110.46	UTC+3h
	MOIU	0.29	35.29	-9.17	107.00	UTC+2h
	MAL2	-3.0	40.19	-12.43	111.86	UTC+3h
Mid-latitude	MZUZ	-11.42	34.01	-21.87	104.92	UTC+2h
	HRAO	-25.89	27.69	-36.32	94.69	UTC+2h
	SUTH	-32.38	20.81	-41.09	84.76	UTC+1h
High latitude	SYOG	-69.00	39.58	-66.08	71.65	UTC+3h

1.2. Method

108 This study focuses on the analysis of the ionospheric response to geomagnetic storms with sudden commencements
109 (SSC) that occurred during the maximum phase of solar cycle 24 (2012–2014). Event selection was based on two
110 main criteria.

111 (1) Storm isolation: only geomagnetic storms with a planetary K_p index ≥ 5 and a minimum Dst index ≤ -50 nT
112 were considered. In addition, magnetically quiet conditions before and after the SSC were required to ensure that the
113 selected storms were isolated events, following the methodology adopted by Azzouzi (2016) and Bazié et al.
114 (2025); (2) Availability of GNSS data: the selection was restricted to events for which ionospheric data were
115 available at all or most of the GNSS stations considered, thereby ensuring sufficient spatial and temporal coverage
116 for a reliable analysis.

117 As a reference, we adopted the mean VTEC computed from the five geomagnetically quietest days of the month
118 corresponding to each storm (Chakraborty et al. 2015; Kuai et al. 2016; Omojola et Adewumi 2019; Sharma et al.
119 2020; Berényi et al. 2023; Sawadogo et al. 2023; Silwal et al. 2023; Uga et al. 2024). The list of these quiet days is
120 available at https://datapub.gfz.de/download/10.5880.Kp.0001/Quiet_Disturbed_Days/.

121 Two complementary approaches were employed. The **qualitative analysis** consists of a direct comparison between
122 storm-time VTEC temporal variations and the mean VTEC of the quiet days, allowing a visual assessment of
123 ionospheric disturbances (positive, negative, or negligible deviations). The **quantitative analysis** is based on the
124 relative VTEC deviation ($\Delta VTEC$, %), expressed as a percentage, in order to accurately quantify the magnitude of
125 the ionospheric perturbations. This deviation is defined as :

$$\Delta VTEC(\%) = \frac{VTEC_S - VTEC_Q}{VTEC_Q} \times 100$$

126 where $VTEC_S$ denotes the daily mean VTEC during storm conditions, and $VTEC_Q$ represents the daily mean VTEC
127 averaged over the five quietest days of the corresponding month.

128 Table 2 summarizes the geomagnetic storms selected for this study, providing the SSC dates, minimum Dst values
129 (Dst_{min}), maximum K_p indices (K_p_{max}), the corresponding season, and the five quietest days of the month. The
130 season during which each storm occurred is specified in order to explain the interhemispheric asymmetry of VTEC.
131 Indeed, the intensity and dominant direction of neutral winds vary with the seasons, leading to significant
132 differences between hemispheres and promoting stronger plasma anomalies in winter than in summer (Astafyeva
133 2009). Therefore, to analyze storm effects as a function of season, the seasons were classified following the method
134 proposed by (Azzouzi 2016). Accordingly, storm events were binned into seasonal categories following this
135 classification scheme: March–April equinox, September–October equinox, summer solstice (May–August), and
136 winter solstice (November–February)

137 **Table 2:** Extreme Dst and K_p values during the selected geomagnetic storms and the quiet days of the
138 corresponding months.

N°	Date of storm	SCC time	K_p (max)	Dst (min)	Season	The five quietest days of the month in order
1	14/07/2012	18:09:00	7	-139	Solstice	13;26;27;18 et 31
2	17/03/2013	05:59:48	7	-132	Equinoxe	08;07;26;25 et 13
3	02/10/2013	01:54:36	8	-72	Equinoxe	05;28;04;19 et 21
4	27/02/2014	16:50:00	5	-97	Solstice	13;26;14;25 et 02

139

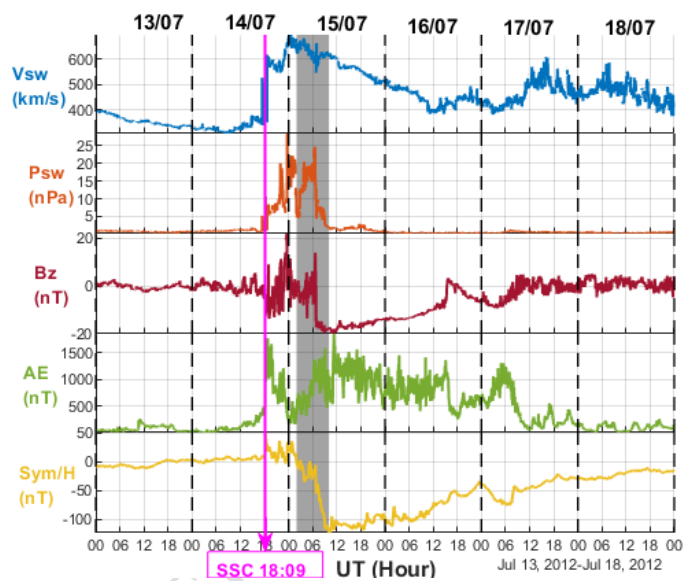
140 2. Results

141 2.1. Evolution of Interplanetary Parameters and Geomagnetic Indices during the Storms

142 Figures 2a–2d show the temporal variations of the solar wind speed (V_{sw} , km s $^{-1}$), solar wind dynamic pressure
143 (P_{sw} , nPa), the south–north component of the interplanetary magnetic field (IMF B_z , nT), the auroral electrojet
144 index (AE, nT), and the symmetric ring current index (SYM/H, nT), with a 1-min temporal resolution, for the
145 periods 13–18 July 2012, 15–20 March 2013, 30 September–5 October 2013, and 26 February–3 March 2014,
146 respectively. In each figure, the vertical magenta line and the shaded area indicate the storm sudden commencement
147 (SSC) and the main phase of the geomagnetic storm, respectively.

148 We first analyze the period from 13 to 18 July 2012 (Fig. 2a). After a magnetically quiet interval, the arrival of the
 149 interplanetary shock (SSC) at 18:09 UT was followed by a rapid increase in solar wind speed, reaching 681.9 km s^{-1} ,
 150 accompanied by strong magnetospheric compression as indicated by a peak dynamic pressure of 28.46 nPa. The
 151 IMF Bz component, initially weak and southward oriented, exhibited oscillations between -20 and $+22 \text{ nT}$ until
 152 about 06:42 UT on 15 July, before remaining persistently southward for nearly 32 hours (until approximately 15:00
 153 UT on 16 July). This prolonged southward orientation favored efficient coupling between the solar wind magnetic
 154 field and the terrestrial magnetosphere.

155 Auroral activity intensified markedly, with the AE index reaching a maximum value of 1772 nT at 18:48 UT on 14
 156 July. The SYM/H index showed an initial positive excursion up to $+51 \text{ nT}$, followed by a sharp decrease to -123 nT
 157 at 10:04 UT on 15 July, marking the end of the storm main phase. This was followed by a gradual recovery phase,
 158 which concluded around 10:00 UT on 18 July.

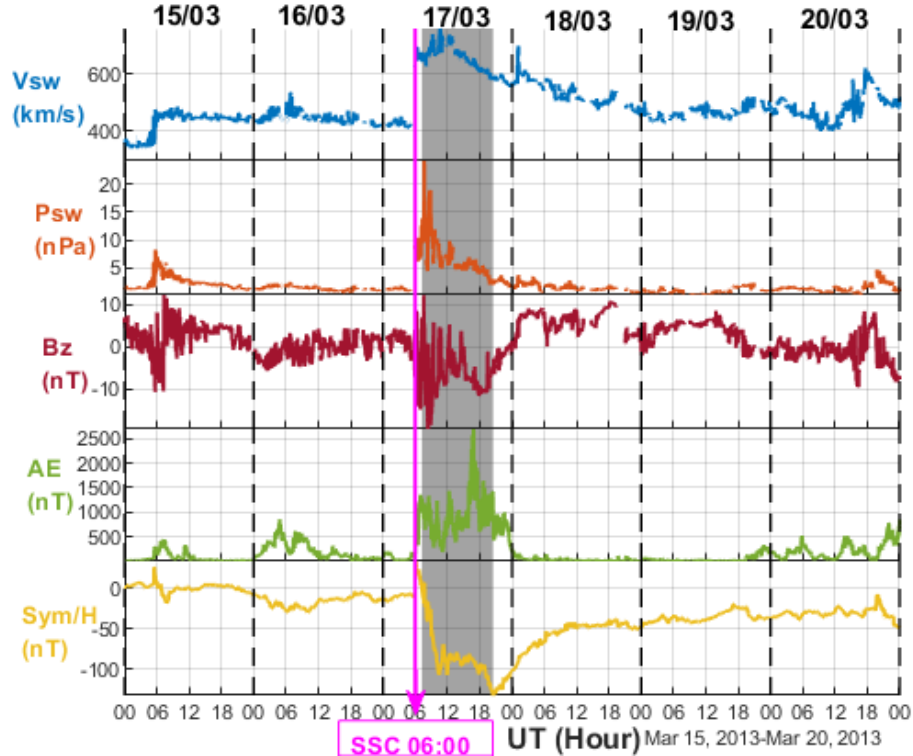


176 Figure 2.a: From top to bottom, it illustrates the temporal variations of Vsw (km/s), Psw (nPa), Bz (nT), AE (nT),
 177 and SYM/H (nT) with a resolution of one minute for the period from July 13 to 18, 2012.

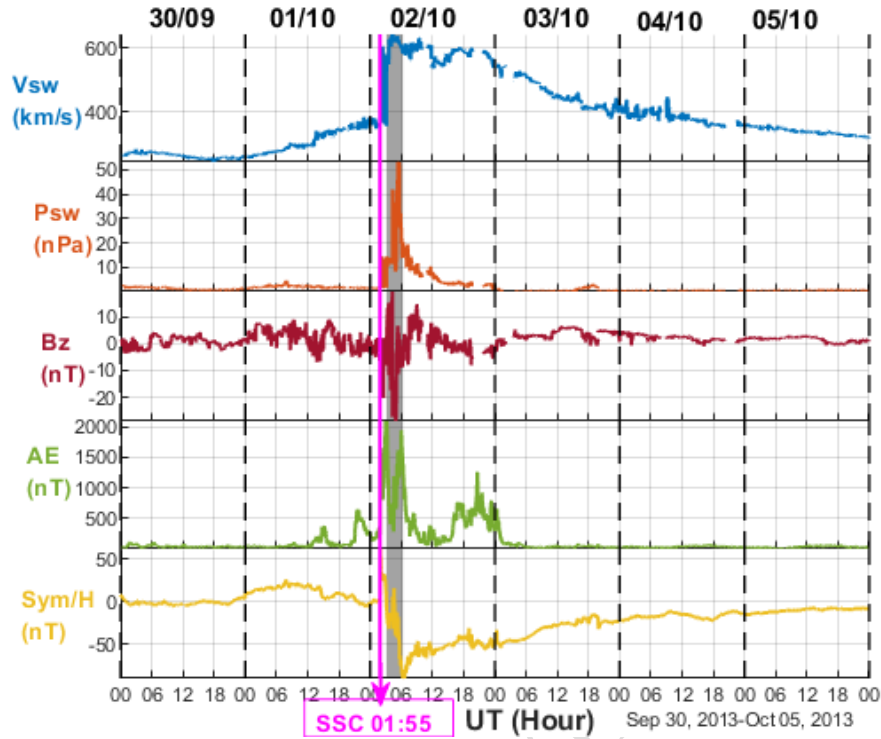
178 On 15 March 2013, at around 06:00 UT, NASA reported the eruption of a magnetic filament near the sunspot region
 179 AR1692. This eruption produced an M1-class solar flare and a coronal mass ejection (CME) directed toward Earth
 180 with an estimated speed of about 900 km s^{-1} (Habyarimana 2023). The CME reached Earth at approximately 06:00
 181 UT on 17 March 2013, triggering an intense geomagnetic storm commonly referred to as the “St. Patrick’s Day
 182 storm” (Yue et al. 2016).

183 Solar wind conditions and geomagnetic activity from 15 to 20 March 2013 are shown in Fig. 2b. As illustrated in the
 184 figure, immediately after the arrival of the solar wind shock, marked by an SSC at 06:00 UT on 17 March 2013, the
 185 solar wind speed increased rapidly, reaching 757.4 km s^{-1} at 10:38 UT, while the dynamic pressure peaked at 24.18
 186 nPa at 07:41 UT and remained above 5 nPa for more than 11 hours. During this interval, the IMF Bz component
 187 oscillated between -19.34 and $+12.22 \text{ nT}$ before turning persistently southward around 15:00 UT.

188 Auroral activity intensified significantly, with the AE index reaching a maximum value of approximately 2689 nT at
 189 16:51 UT, indicating strong auroral current activity. The SYM/H index exhibited an initial positive excursion
 190 followed by a sharp decrease to -132 nT at 20:28 UT on 17 March 2013, marking the end of the storm main phase,
 191 after which a gradual recovery phase extended until 20 March.

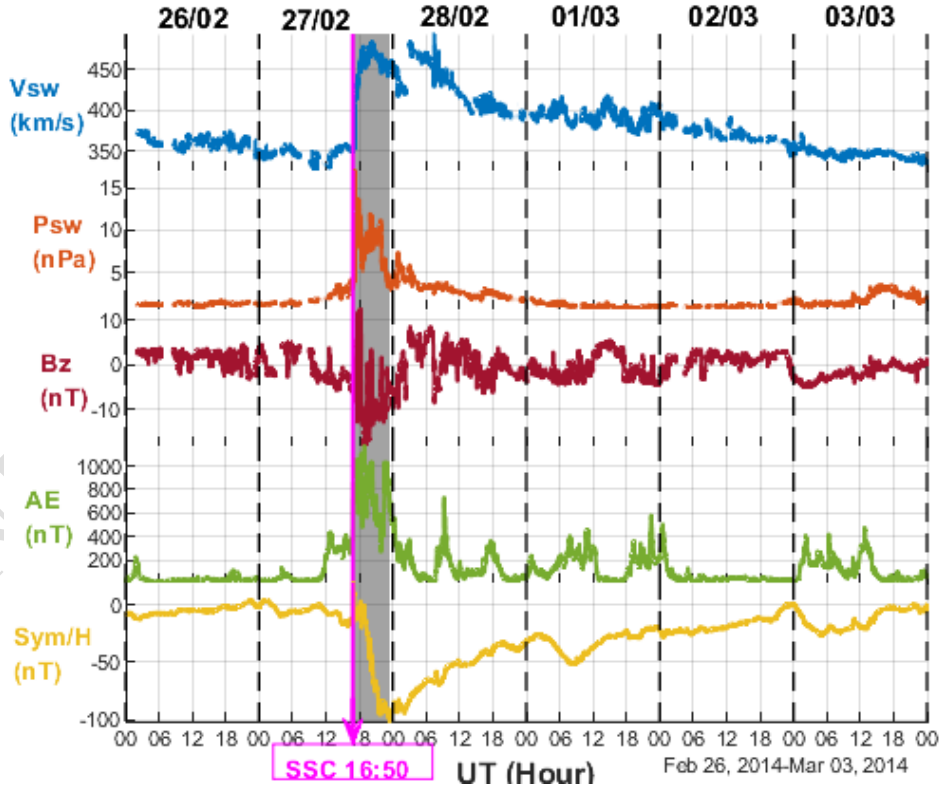


192
 193 Figure 2.b shows, from top to bottom, the temporal variations of V_{sw} (km/s), P_{sw} (nPa), B_z (nT), AE (nT), and
 194 SYM/H (nT) with a resolution of one minute for the period from March 15 to 20, 2013.
 195 The panels of Fig. 2c (from top to bottom) illustrate the evolution of solar wind and geomagnetic parameters from
 196 30 September to 5 October 2013. On 2 October, immediately after the SSC, the solar wind speed abruptly increased
 197 from 363.4 km s^{-1} to more than 644 km s^{-1} at 04:15 UT, while the solar wind dynamic pressure (P_{sw}) rose from 1.62
 198 nPa to a maximum value of 53.17 nPa at 05:25 UT, indicating the arrival of a solar particle cloud. During this
 199 interval, the IMF B_z component exhibited strong fluctuations between 02:00 and 05:00 UT before turning northward
 200 and returning to near-normal levels.
 201 The AE index showed a sharp increase, reaching a first peak of 2089 nT at 02:59 UT, then decreasing below 300 nT
 202 around 04:30 UT, before displaying a second peak of 1941 nT at 06:00 UT. Later, AE increased again to 1259 nT
 203 around 20:30 UT before returning to quiet values toward the end of the storm. The SYM/H index initially increased
 204 to 62 nT at 01:58 UT, then dropped to a minimum of -90 nT at 06:19 UT, with a brief positive excursion around
 205 04:30 UT, followed by a gradual recovery.
 206 The geomagnetic storm of 27 February 2014 was most likely caused by a coronal mass ejection (CME) associated
 207 with the solar eruption of 25 February 2014. Solar wind conditions and geomagnetic activity from 26 February to 3
 208 March 2014 are shown in Fig. 2d. Immediately after the SSC at 16:50 UT on 27 February, the solar wind speed
 209 increased from 350 km s^{-1} to 482.8 km s^{-1} at 20:16 UT, while the dynamic pressure reached 17.02 nPa at 17:11 UT.
 210 The IMF B_z component fluctuated between -18 and $+12 \text{ nT}$, remaining predominantly southward until about 02:00
 211 UT on 28 February. During this period, the AE index reached a maximum value of 1171 nT at 18:54 UT before
 212 returning to near-quiet levels around 05:00 UT on 28 February, with sporadic enhancements persisting until 3
 213 March. The SYM/H index initially increased to $+19 \text{ nT}$ and then dropped to -101 nT at 23:24 UT, marking the end
 214 of the storm main phase, followed by a gradual recovery with minor fluctuations until quiet conditions were restored
 215 on 3 March.
 216



217
218
219

Figure 2c: From top to bottom, temporal variations of V_{sw} (km s^{-1}), P_{sw} (nPa), B_z (nT), AE (nT), and SYM/H (nT) at a 1-minute resolution for the period 30 September–5 October 2013.



220
221
222
223

Figure 2d: From top to bottom, temporal variations of V_{sw} (km s^{-1}), P_{sw} (nPa), B_z (nT), AE (nT), and SYM/H (nT) at a 1-minute resolution for the period 26 February–3 March 2014.

2.2. VTEC Response to Geomagnetic Storms

224 To analyze the ionospheric response to geomagnetic storms, three complementary representations were used.
225 Station-by-station VTEC time series highlight local variability by comparing disturbed conditions with quiet-day
226 levels expressed in TECU. Spatio-temporal VTEC maps provide a regional view of ionospheric dynamics and
227 storm-time responses. The relative deviation Δ VTEC is computed as the difference between daily VTEC values and
228 the mean VTEC of the five quietest days of the corresponding month. These regional VTEC and Δ VTEC maps were
229 generated using MATLAB-based graphical routines.

230 In the station-by-station overlays, stations are ordered from top to bottom according to decreasing latitude from
231 north to south. The red curve represents storm-time VTEC, the blue curve corresponds to the mean VTEC of the five
232 quiet days, and the light-blue shaded band indicates a $\pm 20\%$ variability range around the quiet-day mean. The
233 vertically shaded gray areas delimit the storm main phase. The spatio-temporal maps display absolute VTEC values
234 and relative deviations Δ VTEC as a function of universal time, for latitudes between -75° and 75° and longitudes
235 between 20° E and 40° E. The vertical magenta line marks the SSC onset time in each figure.

236 **2.2.1. The 14 July 2012 Storm**

237 Figures 3a–3c respectively show the VTEC variations, the spatio-temporal VTEC maps, and the relative deviation
238 Δ VTEC (%) for the period 13–18 July 2012.

239 In Fig. 3a, between 13 and 14 July, prior to storm onset, all stations—except RAMO and ANKR, located near the
240 boundary between low and mid-northern latitudes, which exhibited a slight increase just before storm onset—
241 display a typical diurnal VTEC cycle: a gradual morning increase, a local midday maximum that is more
242 pronounced at low latitudes (e.g., 44.62 TECU at ADIS on 13 July) than at high latitudes (9.58 TECU at SYOG),
243 followed by an evening decrease to nocturnal minima. During this period, VTEC curves remain within the error
244 band around the reference, confirming the absence of significant ionospheric disturbances prior to storm onset.

245 After the SSC, no clear anomaly is observed until around 23 UT on 14 July. At that time, stations near the equatorial
246 ionization anomaly (EIA) trough, such as NAMA, ADIS, and MOIU, record a slight VTEC depletion, while stations
247 located near the EIA crests (RAMO, MZUZ) show a moderate enhancement.

248 On 15 July, maximum VTEC values increased significantly compared to the quiet reference and the pre-storm days,
249 except at ADIS, located near the equatorial trough, where the maximum value (48.6 TECU) remained comparable to
250 the reference (48.8 TECU). The VTEC enhancement is particularly pronounced in the Southern Hemisphere. For
251 instance, SUTH recorded a maximum of 37.7 TECU on 15 July, compared to 19.2 TECU for the quiet reference,
252 corresponding to an increase of 18.5 TECU, and 17.3 TECU on 14 July, representing a 20.4 TECU increase relative
253 to the previous day. In contrast, ADIS and MOIU exhibit a simultaneous trough when maxima are recorded
254 elsewhere.

255 During the night of 15–16 July, before 00 UT, low-latitude stations in the Northern Hemisphere register a decrease
256 in VTEC, while those in the Southern Hemisphere show an increase. At 00 UT, all stations reach minimum values,
257 with a particularly strong decrease at ADIS, located within the anomaly trough. Between 16 and 18 July, high-
258 latitude stations in both hemispheres display VTEC values lower than the quiet reference, followed by a gradual
259 recovery on 18 July. At mid- and low latitudes, an interhemispheric asymmetry is evident: in the Northern
260 Hemisphere, only weak VTEC fluctuations persist until 18 July, whereas in the Southern Hemisphere, more
261 pronounced enhancements appear on 16 July before a gradual recovery. For example, at ANKR, the maximum
262 VTEC on 16 July reaches 27.5 TECU compared to 25.3 TECU for the reference (+2.2 TECU), while at MAL2 the
263 maximum reaches 54.7 TECU compared to 33.9 TECU for the reference, corresponding to an increase of 20.8
264 TECU.

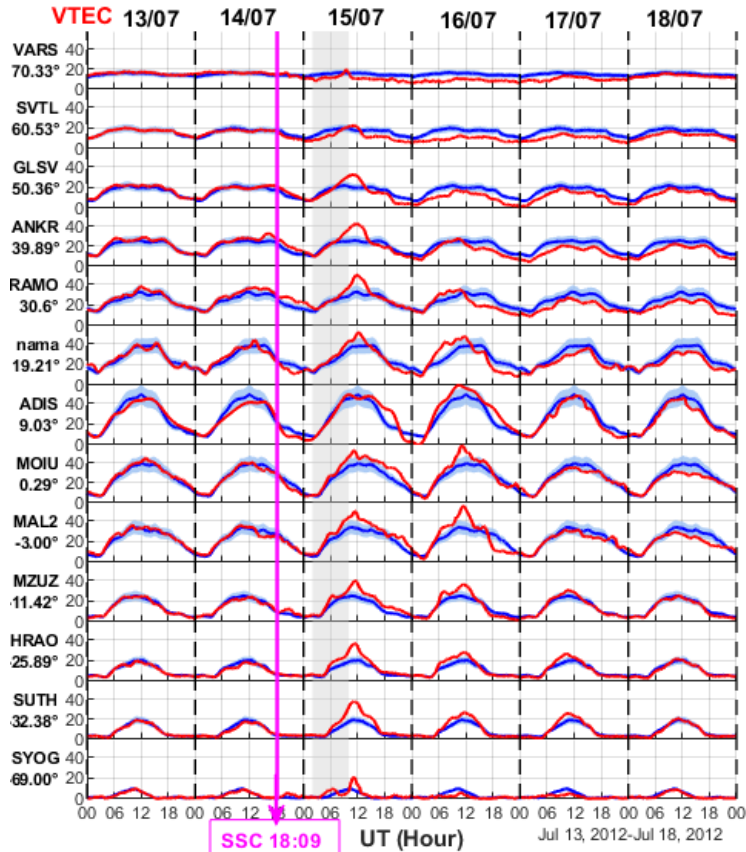


Figure 3a: VTEC variations during 13–18 July 2012.

Figure 3b highlights a marked intensification of the equatorial ionization anomaly (EIA) on 15 July, characterized by two crests extending toward higher latitudes. On 16 July, VTEC values around the magnetic equator increase significantly compared to 15 July, accompanied by a weakening of the EIA structure. From 17 to 18 July, maximum VTEC values gradually recenter around the magnetic equator and decrease in intensity until 18 July.

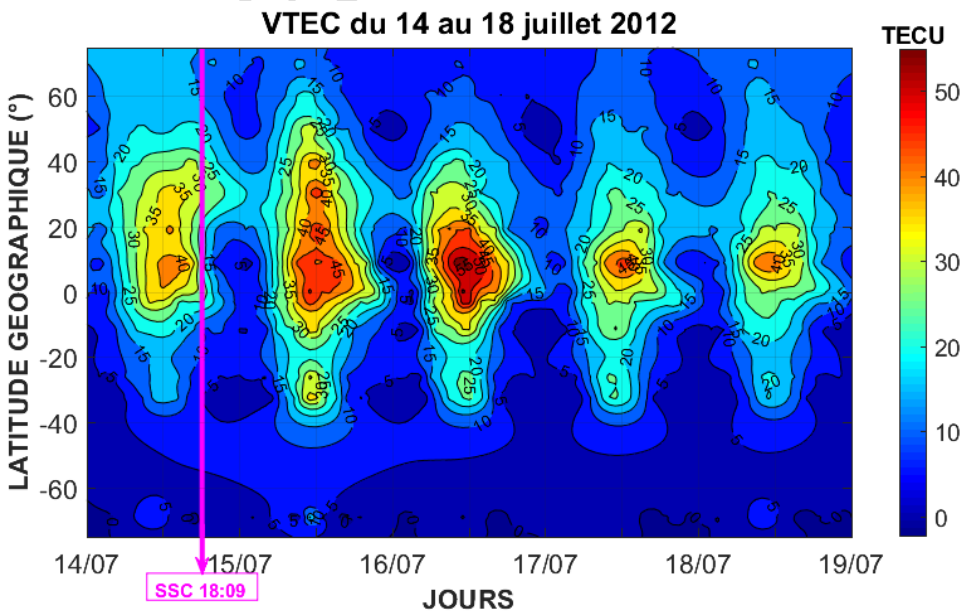
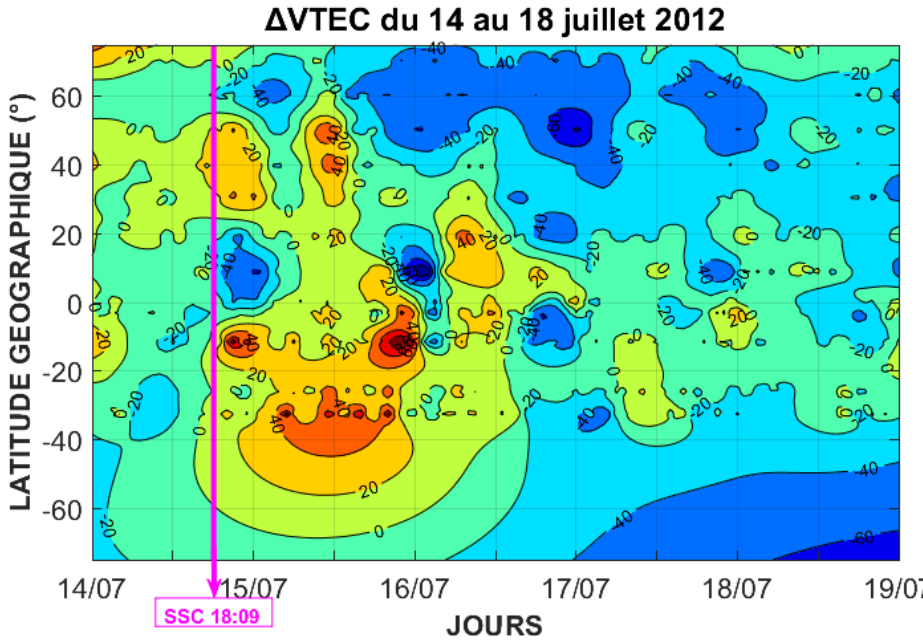


Figure 3b: VTEC map for the period 14–18 July 2012.

273 Figure 3c reveals several significant Δ VTEC enhancements, particularly around 10°S latitude near 19 UT on 14 and
 274 15 July, reaching about 40% and 80%, respectively, as well as at mid-latitudes in both hemispheres around local
 275 noon on 15 July, with increases of approximately 40%. The figure also shows pronounced Δ VTEC decreases
 276 (negative ionospheric storm phase) in the equatorial region around 01 UT on 15 and 16 July, reaching -40% and
 277 -80%, respectively, and at high latitudes in both hemispheres, where reductions range between -40% and -60%.
 278 During the storm, Δ VTEC enhancements are more pronounced in the Southern Hemisphere than in the Northern
 279 Hemisphere, while depletions are stronger in the Northern Hemisphere. This behavior is consistent with the seasonal
 280 context of the storm, which occurred near the solstice, corresponding to summer in the Northern Hemisphere and
 281 winter in the Southern Hemisphere.



282

283 **Figure 3c:** Relative Δ VTEC deviation map for 14–18 July 2012.

2.2.2 The 17 March 2013 Storm

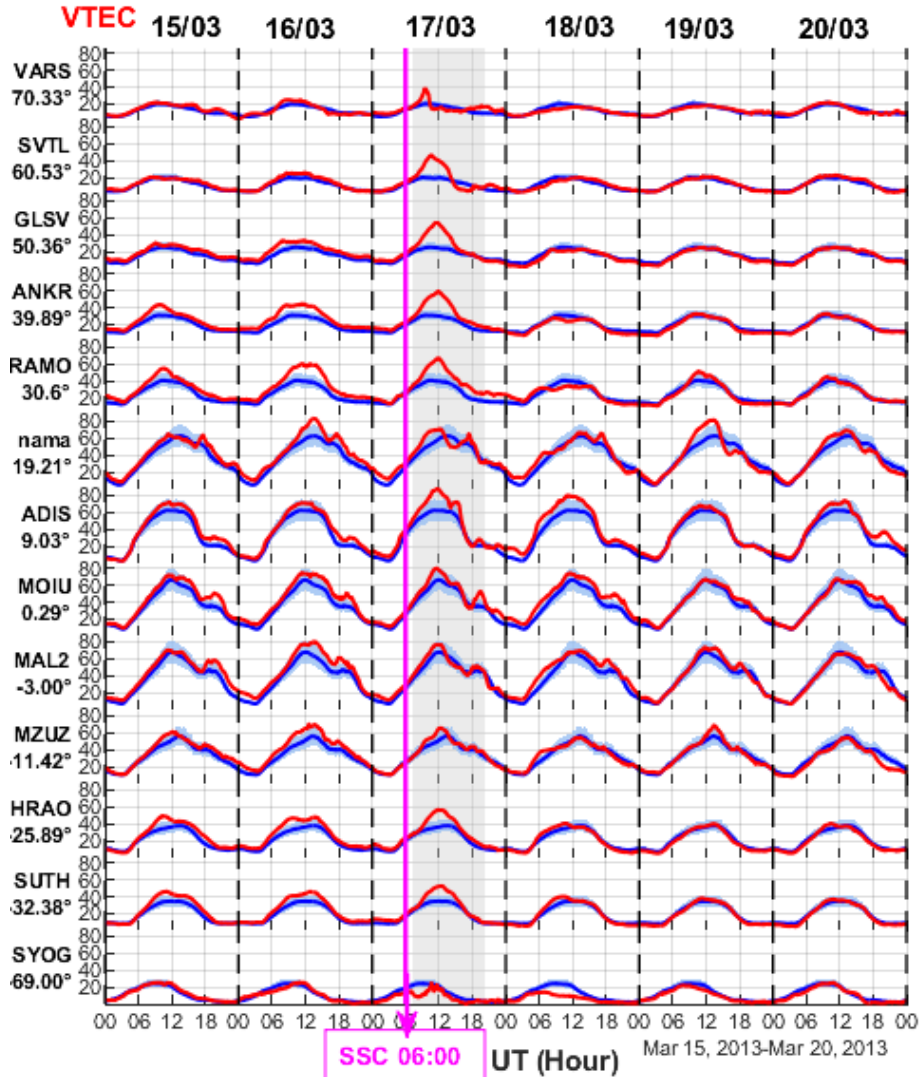
285 Figures 4a–4c respectively illustrate the VTEC variations, the spatiotemporal VTEC maps, and the relative deviation
 286 Δ VTEC (%) for the period from 15 to 20 March 2013.

287 Figure 4a shows the VTEC variations between 15 and 20 March 2013. On 16 March, the day preceding the storm
 288 and considered geomagnetically quiet, the maximum VTEC values at all stations are higher than the reference
 289 values, with increases ranging from +1.4 TECU at SYOG (25.7 TECU compared to 24.3 TECU for the reference) to
 290 +20.2 TECU at NAMA (82.4 TECU compared to 62.2 TECU for the reference).

291 On 17 March, during the storm main phase, all stations record maximum VTEC values higher than the reference,
 292 except for SYOG (southern high latitude). The most pronounced increases are observed at northern high latitudes
 293 and at northern and southern mid-latitudes, as well as at stations located near the magnetic equator (ADIS, MOIU),
 294 with enhancements ranging from +13.6 TECU (MOIU) to +28.6 TECU (ANKR) relative to the reference, and from
 295 +5.5 TECU (MOIU) to +20.7 TECU (GLSV) relative to 16 March. In contrast, stations located near the crests of the
 296 equatorial ionization anomaly (EIA) (NAMA, MAL2, MZUZ) show weak increases relative to the reference and
 297 slight decreases compared to 16 March, indicating an inhibition of the EIA.

298 During the recovery phase, 18 March is characterized by contrasting responses: most stations exhibit weak VTEC
 299 fluctuations, whereas ADIS and SYOG show, respectively, a strong increase and a pronounced decrease (ADIS:
 300 79.1 TECU versus 61.8 TECU for the reference, i.e., +17.3 TECU; SYOG: 14.5 TECU versus 24.3 TECU, i.e., -9.8
 TECU). On 19 March, stations located near the EIA crests record increases exceeding +10 TECU relative to the

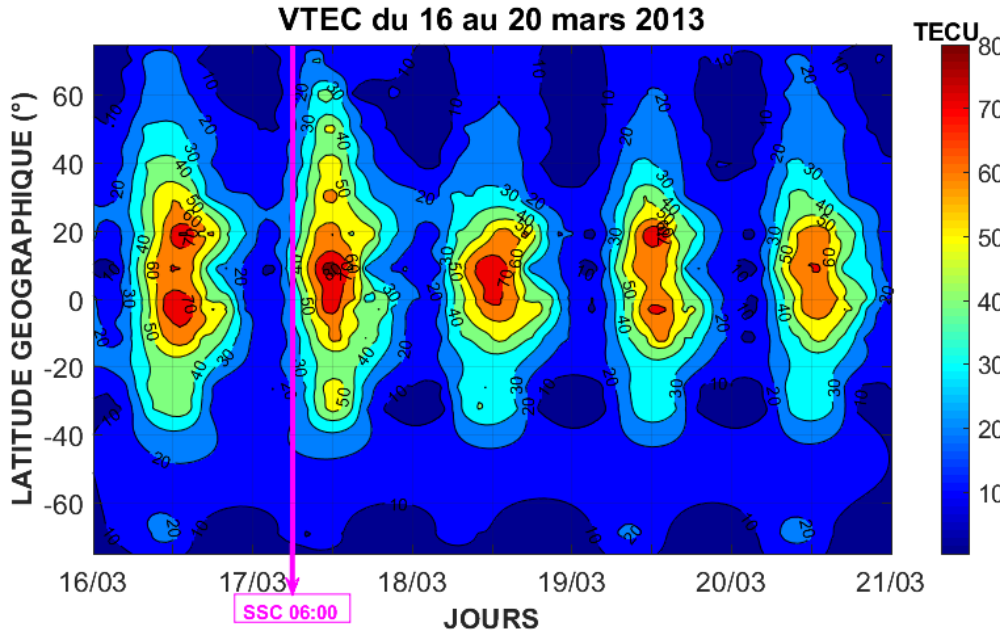
302 reference, notably RAMO (+10.4 TECU), NAMA (+18.5 TECU), and MZUZ (+12.0 TECU), reflecting a
 303 strengthening of the EIA. Finally, on 20 March, all stations return to values comparable to quiet conditions,
 304 indicating a recovery of the ionosphere, except at ADIS where an increase of +11.2 TECU is still observed.



305

306 Figure 4a: VTEC variation during the period from 15 to 20 March 2013.

307 Figure 4b shows that on 16 March, the day preceding the storm, two well-defined crests of the equatorial ionization
 308 anomaly (EIA) are clearly visible. In contrast, on 17 March, the storm day, these crests disappear, accompanied by
 309 an increase in VTEC around the magnetic equator, at northern and southern mid-latitudes—more pronounced in the
 310 Northern Hemisphere—and at northern high latitudes. On 18 March, the crests remain absent, and a decrease in
 311 VTEC is observed at all latitudes compared to 17 March, with a particularly strong reduction at northern mid-
 312 latitudes. On 19 March, the EIA crests reappear, with the northern crest being more developed than the southern
 313 one. Finally, on 20 March, the crests disappear again, while an increase in VTEC is observed around the magnetic
 314 equator.

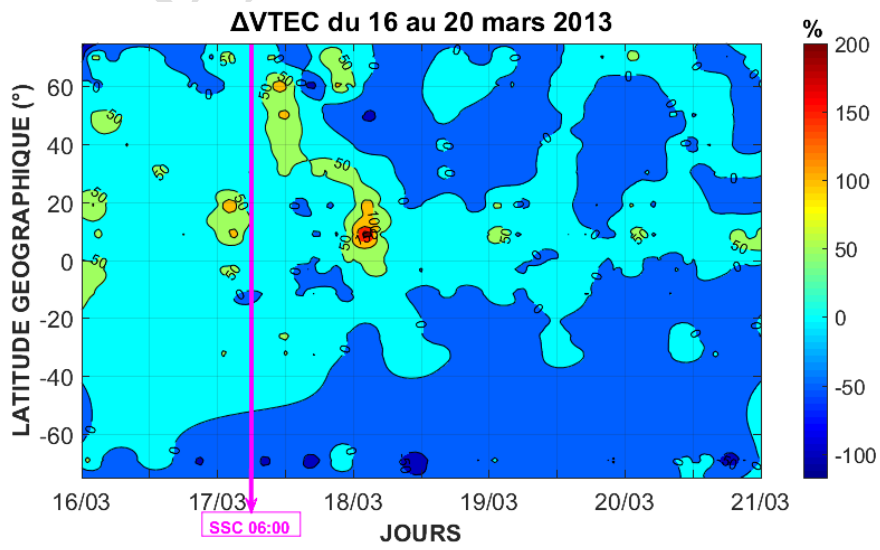


315

316

Figure 4b: VTEC map during the period from 16 to 20 March 2013.

317 Figure 4c highlights several significant increases (Δ VTEC $> +50\%$) around 01 UT, located at the EIA crests and at
 318 northern mid-latitudes, around 04 UT and 14 UT on 16 March, the day preceding the storm. On 17 March, the storm
 319 day, a marked positive ionospheric storm appears around 01 UT, prior to the storm onset at 06 UT, with Δ VTEC
 320 values exceeding $+100\%$ near the magnetic equator. During the main phase, substantial VTEC enhancements are
 321 also observed around 12 UT at northern mid-latitudes. After 12 UT, the positive ionospheric storm progressively
 322 extends from northern mid-latitudes toward low latitudes, reaching the magnetic equator around 22 UT, where the
 323 positive effect intensifies strongly around 01 UT on 18 March, with Δ VTEC values reaching up to $+200\%$. Around
 324 22 UT on 17 March, an increase is also observed at northern high latitudes. Finally, on 19 and 20 March, strong
 325 positive deviations (Δ VTEC $> +50\%$) persist only near the magnetic equator around 01 UT each day, while negative
 326 deviations appear at southern high latitudes on 18 March around 10 UT.



327

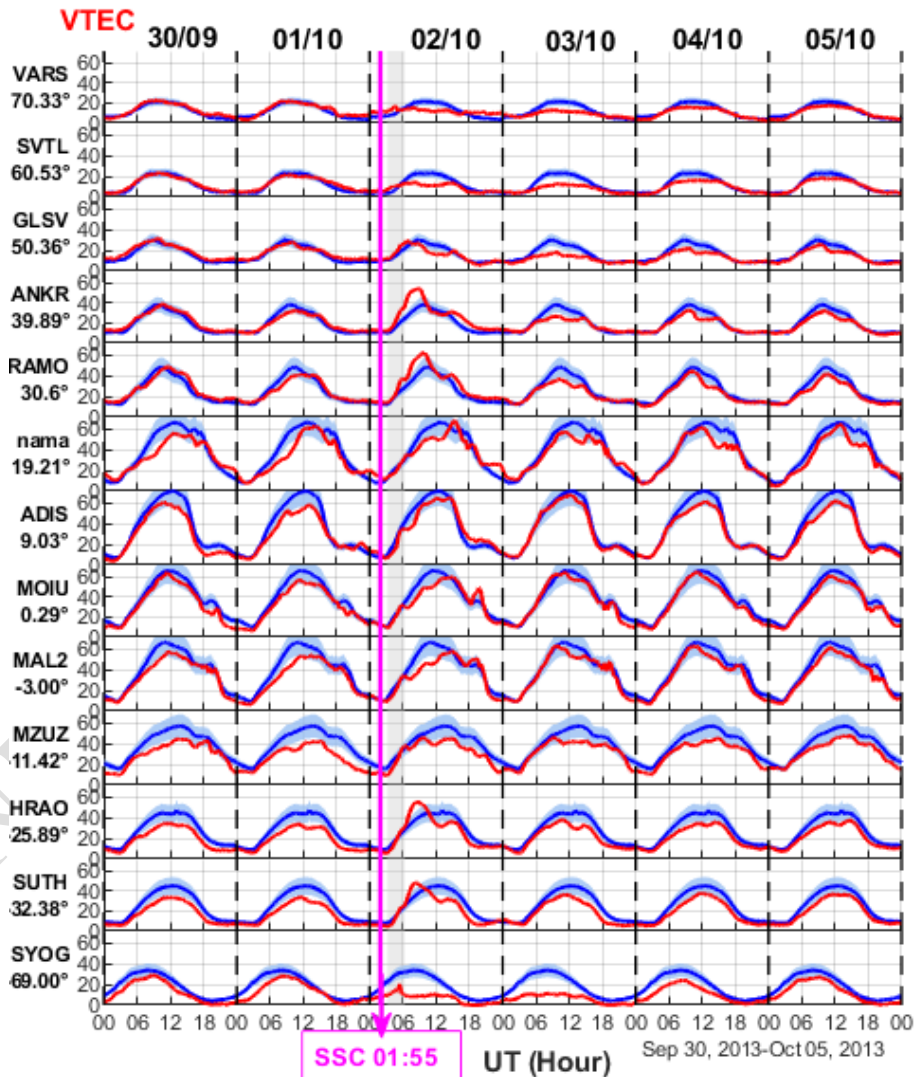
328

Figure 4c: Map of the relative deviation Δ VTEC during the period from 16 to 20 March 2013.

329 **3.2.3 The 02 October 2013 Storm**

330 Figure 5a presents the VTEC variations from 30 September to 5 October 2013. On 1 October, a geomagnetically
 331 quiet day, the maximum VTEC values recorded at all stations decreased relative to the reference, with differences
 332 ranging from -1.8 TECU to -14.7 TECU (SVTL: -1.8 TECU; MZUZ: -14.7 TECU), except for the VARS station,
 333 whose maximum value (21.9 TECU) remains comparable to the reference (21.3 TECU).

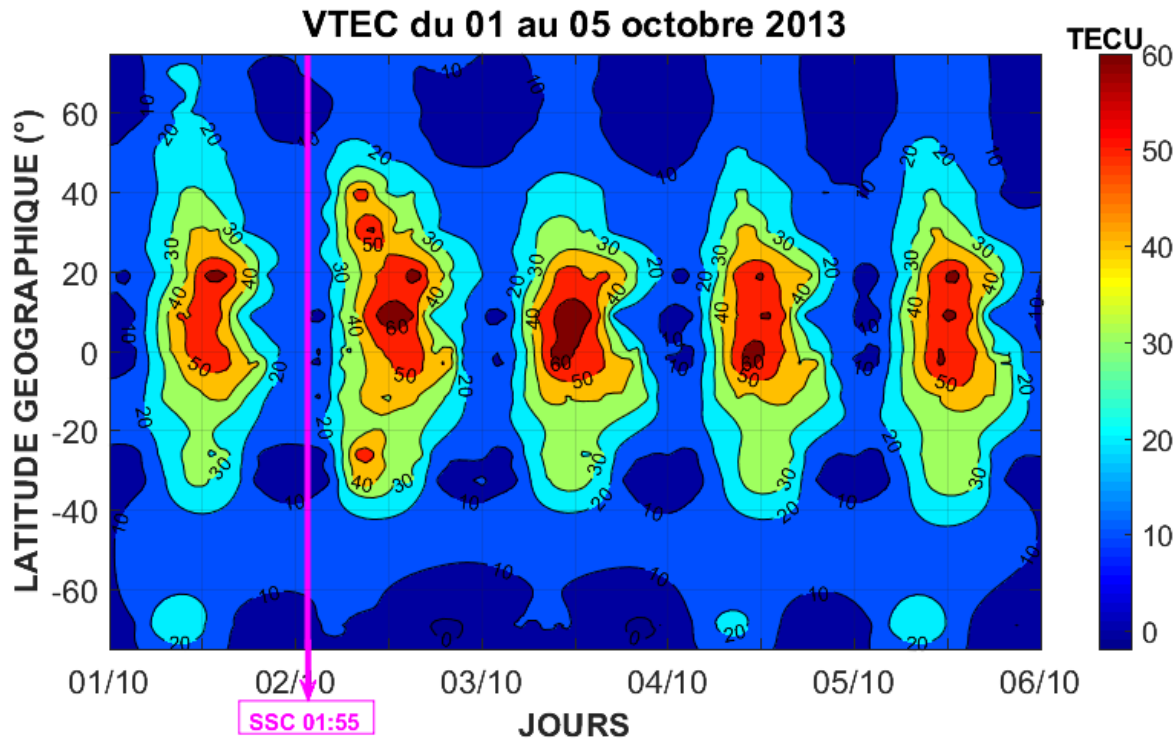
334 On 2 October, the storm day, stations located at northern and southern mid-latitudes exhibit a clear increase in
 335 maximum VTEC values relative to the quiet reference and to the days preceding the storm, with peaks occurring
 336 mainly between 06 UT and 12 UT. These increases are more pronounced in the Northern Hemisphere, particularly at
 337 ANKR (+16.0 TECU) and RAMO (+13.9 TECU), compared to +7.7 TECU at HRAO and +3.2 TECU at SUTH in
 338 the Southern Hemisphere. Low-latitude stations do not show notable variations but display oscillatory VTEC
 339 behavior. In contrast, at northern and southern high latitudes, a decrease in maximum VTEC values relative to the
 340 reference is observed, particularly at SYOG (-13.3 TECU) and, to a lesser extent, at VARS (-4.2 TECU). During
 341 the evening of 2 October, between 18 UT and 00 UT, a slight increase in VTEC is observed in the Northern
 342 Hemisphere. From 3 to 5 October, the maximum VTEC values decrease each day relative to the quiet reference,
 343 with more pronounced reductions at high and mid-latitudes in both hemispheres.



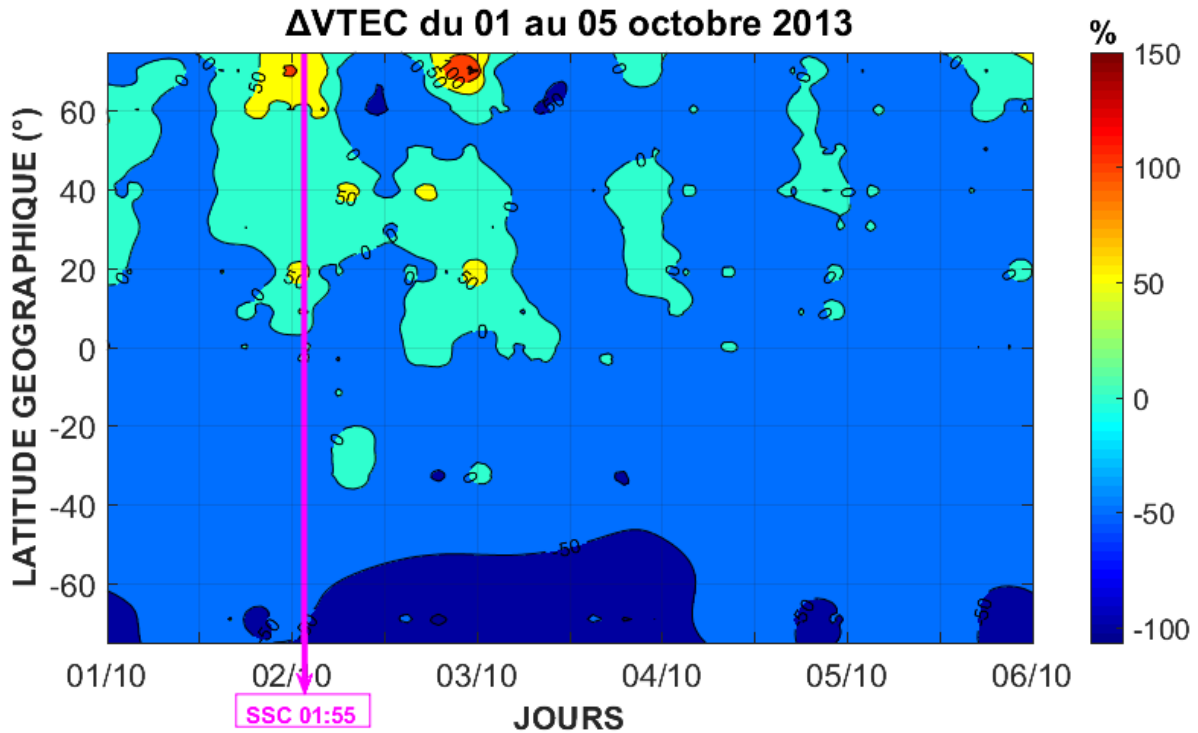
344

345 Figure 5a: VTEC variation during the period from 30 September to 5 October 2013.

346 Figure 5b illustrates that on the quiet day preceding the geomagnetic storm (1 October), a VTEC peak of about 60
 347 TECU is located at the northern crest of the equatorial ionization anomaly (EIA). On 2 October, the storm day, a
 348 strong increase in VTEC (approximately 50 TECU) is observed at northern and southern mid-latitudes as well as at
 349 the magnetic equator (about 60 TECU), with peaks first occurring at mid-latitudes and subsequently at the equator.
 350 On 3 October, the VTEC intensifies around the magnetic equator, forming a broadened band, while the EIA crests
 351 are inhibited. On 4 and 5 October, peaks reappear both in the trough region and at the EIA crests, accompanied by a
 352 slight northward expansion of the enhanced VTEC.



353
 354 Figure 5b: VTEC map during the period from 1 to 5 October 2013.
 355 Figure 5c highlights a pronounced positive ionospheric storm (Δ VTEC $> +50\%$) around 00 UT on 2 October, just
 356 before the storm onset at 01:55 UT, localized at northern high latitudes and at the position of the northern EIA crest.
 357 After the storm onset, around 08 UT and 16 UT, positive deviations of similar magnitude (Δ VTEC $> +50\%$) are
 358 observed at northern mid-latitudes. During the night of 2–3 October, between 22 UT and 01 UT, the deviation
 359 becomes positive again at northern high latitudes (Δ VTEC $> +100\%$) as well as at the northern EIA crest (Δ VTEC $>$
 360 $+50\%$). In contrast, at southern high latitudes, strong negative values (Δ VTEC $< -50\%$) are present between 2 and 4
 361 October, as well as around 18 UT on 1, 4, and 5 October. Similar negative Δ VTEC values (Δ VTEC $< -50\%$) are
 362 also observed at northern high latitudes around 12 UT on 2 October and around 11 UT on 3 October.
 363 The evolution of TEC deviations, characterized by more pronounced positive values in the Northern Hemisphere
 364 and negative values in the Southern Hemisphere, clearly indicates an interhemispheric asymmetry in the ionospheric
 365 response to the geomagnetic storm.



366
367 Figure 5c: Map of the relative deviation Δ VTEC during the period from 1 to 5 October 2013.

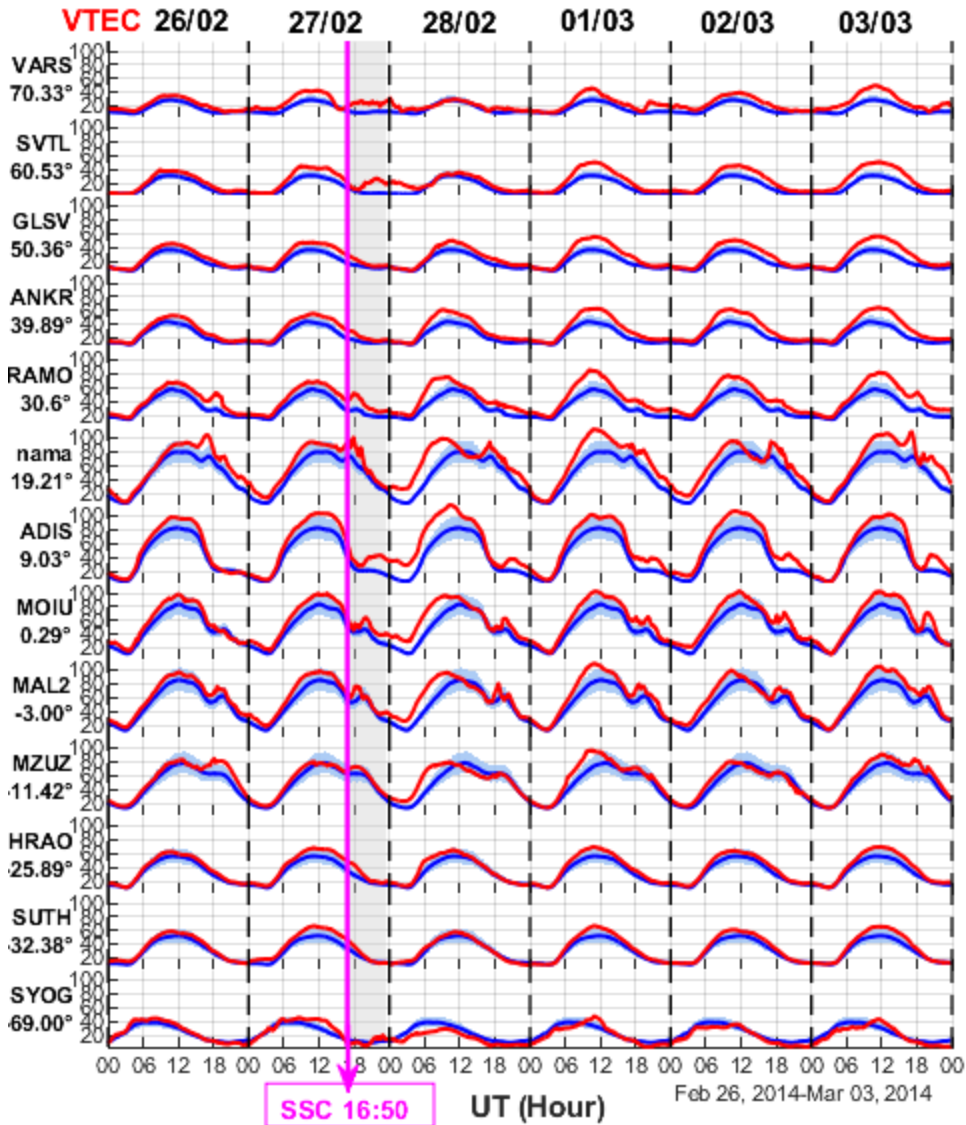
368 2.2.4 The storm of February 27, 2014

369 Figure 6.a illustrates the variations in VTEC between February 26 and March 3, 2014. On February 26 and 27,
370 before the storm began, the maximum VTEC values were already higher than those on calm days for all stations,
371 with increases ranging from +5.7 to +24.3 TECU. The magnetic storm began on February 27 at 16:50 UT. A few
372 hours later, around 23 UT, a sharp increase in VTEC was observed, first at high northern latitudes, then in the
373 equatorial region.

374 On February 28, most stations still recorded maximum VTEC values higher than those of the calm reference (from
375 +2.3 to +32.9 TECU), with the exception of MZUZ, whose maximum value (78.7 TECU) remained comparable to
376 that of the calm day (77.8 TECU), and SYOG, which showed a notable decrease of -9.1 TECU (29.4 TECU
377 compared to 38.5 TECU in calm conditions). These positive effects are much more pronounced in the northern
378 hemisphere. In low latitudes, there is also a time shift in the VTEC peak, which is reached earlier than on calm days.
379 In contrast, in high latitudes, February 28 is characterized by a decrease in maximum VTEC values compared to
380 February 27.

381 On March 1, all stations recorded a further significant increase in maximum VTEC values, ranging from +8.3 TECU
382 (SYOG) to +32.5 TECU (NAMA), with a particularly pronounced intensification in the northern hemisphere. On
383 March 2, VTEC remains above the calm reference in the northern hemisphere, while the increase becomes
384 negligible in the southern hemisphere, even negative at high latitudes (SYOG: 35.7 TECU versus 38.5 TECU, or -
385 2.8 TECU). Finally, on March 3, the maximum VTEC values increased again compared to the reference, with the
386 intensity once again stronger in the northern hemisphere (e.g., +28.8 TECU at NAMA compared to +4.2 TECU at
387 SYOG).

388 Overall, this trend clearly highlights a persistent hemispheric asymmetry in VTEC, which was already present
389 before the magnetic storm began and amplified throughout the storm.

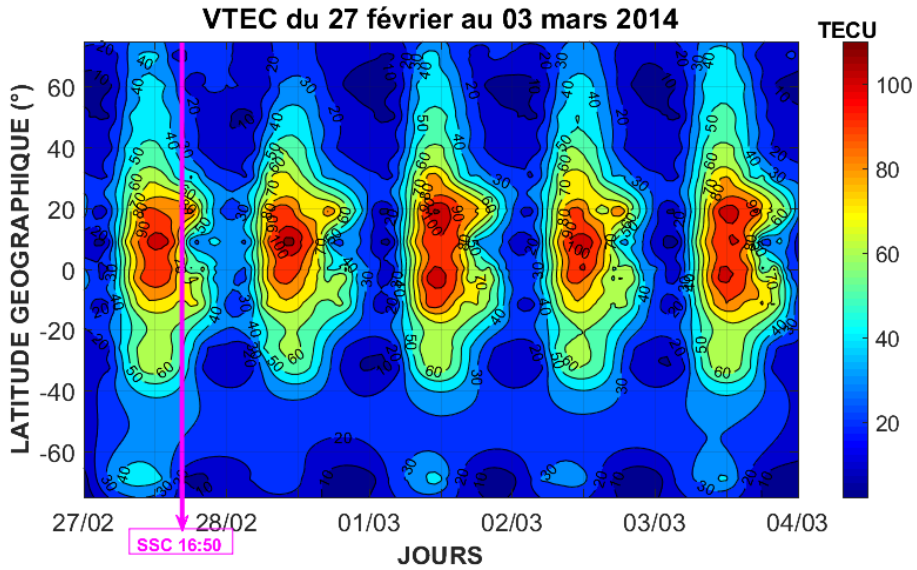


390

391 Figure 6.a: VTEC variation during the period from February 26 to March 3, 2014

392 Figure 6.b shows that on February 27, before the storm began, VTEC values were high (around 100 TECU) centered
 393 on the magnetic equator, while the peaks of the equatorial ionospheric anomaly (EIA) were absent. On February 28,
 394 an intensification of VTEC is observed at the equator, with values exceeding 100 TECU, still accompanied by a
 395 disappearance of the peaks. At the same time, a decrease in VTEC is visible at high and mid northern and southern
 396 latitudes, compared to February 27 and March 1.

397 On March 2, the behavior observed on February 27 persisted but was less pronounced. However, March 1 and 3
 398 were notable for the reappearance of the EIA ridges and their marked intensification. A hemispheric asymmetry is
 399 also visible, both in intensity and extent. For example, on March 1, the northern ridge of the EIA reaches VTEC
 400 values greater than 100 TECU, while the southern ridge has values close to 100 TECU. On March 1 and 3, the
 401 southern crest appears narrower than that of the northern hemisphere, confirming this ionospheric asymmetry.



402

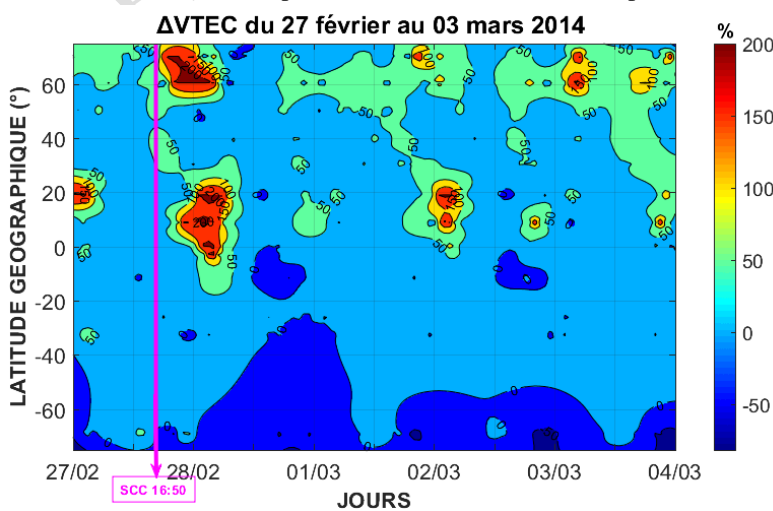
403

Figure 6.b: VTEC map for the period from February 27 to March 3, 2014

404 Figure 6.c reveals a marked positive ionospheric storm, with a Δ VTEC of approximately +100% on February 27 at
 405 around 01 UT at the position of the northern crest of the EIA. During the night of February 27 to 28, very intense
 406 positive variations were observed at high northern latitudes and around the magnetic equator, at around 00 UT and
 407 02 UT respectively, with a Δ VTEC reaching up to +200%. The deviation was already positive at high northern
 408 latitudes, with a Δ VTEC of approximately +50% even before the magnetic storm began, then intensified sharply
 409 during the magnetic disturbance and spread towards the magnetic equator.

410 At high northern latitudes, positive deviations with Δ VTEC values between +50% and +100% are visible from
 411 February 28 to March 3, except during the day around 12 UT on February 28 and a few hours before 12 UT on
 412 March 2. Over the same period, deviations are positive around the magnetic equator, mainly during the night, with
 413 Δ VTEC varying between +50% and +100%. In contrast, the deviation is strongly negative (Δ VTEC around -50%)
 414 only on March 2, at high southern latitudes, around 22 UT.

415 All of these changes clearly highlight a hemispheric asymmetry: positive ionospheric disturbances are more
 416 pronounced and persistent in the northern hemisphere than in the southern hemisphere.



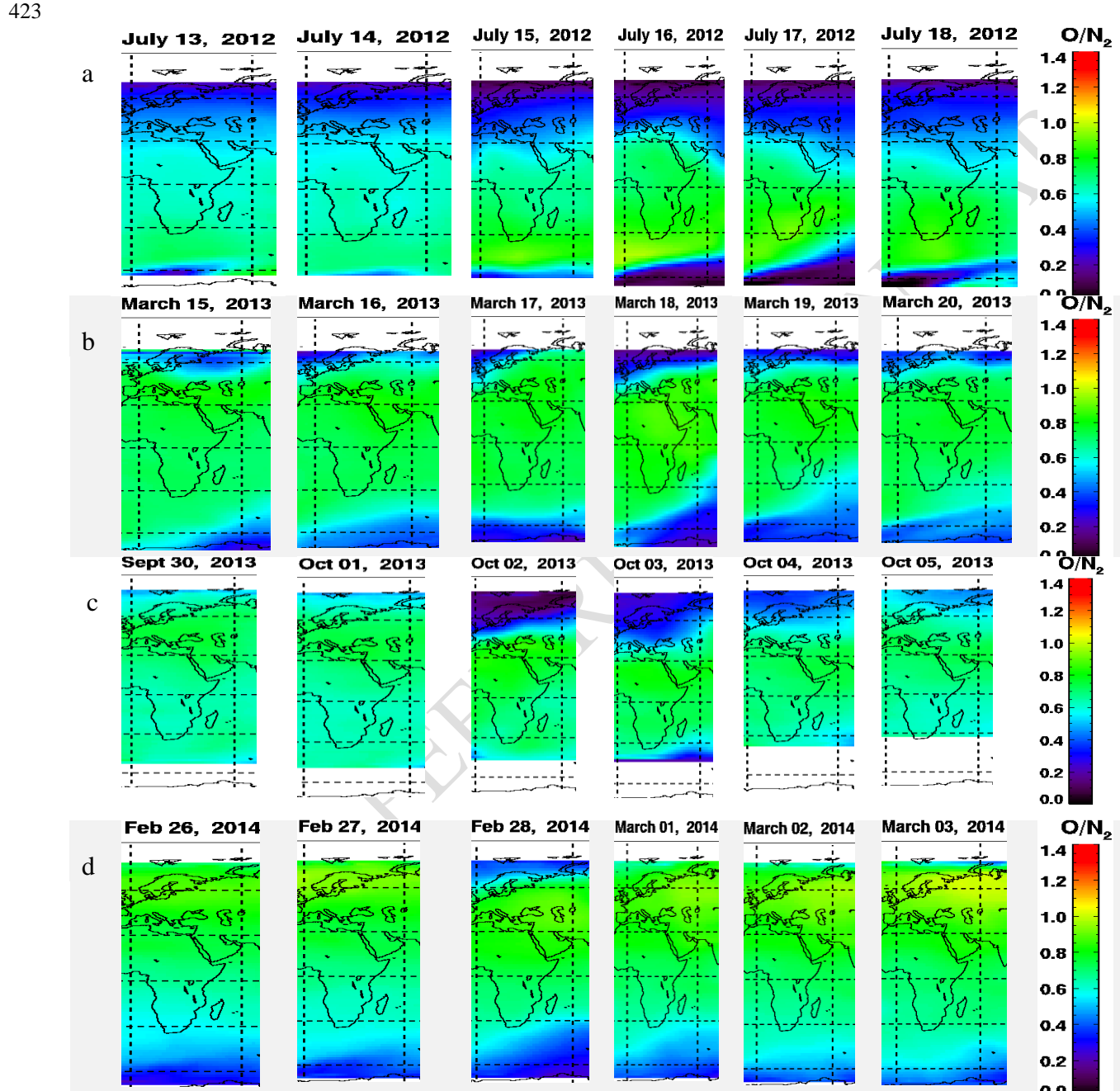
417

418

Figure 6.c: Map of relative deviation Δ VTEC from February 27 to March 3, 2014

419 **2.3. Satellite Data**

420 Figures 7a–7d present the global variations of the thermospheric O/N₂ ratio derived from observations by the Global
 421 Ultraviolet Imager (GUVI) onboard the TIMED satellite during the geomagnetic storms of 13–18 July 2012, 15–20
 422 March 2013, 30 September–5 October 2013, and 26 February–3 March 2014.



425 **Figure 7 (a–d):** Thermospheric O/N₂ ratio derived from GUVI/TIMED observations during the geomagnetic storms
 426 of 13–18 July 2012, 15–20 March 2013, 30 September–5 October 2013, and 26 February–3 March 2014.

427 Analysis of GUVI-derived O/N₂ maps at the GNSS station locations reveals, for each storm, a pronounced depletion
 428 at high latitudes followed by a gradual equatorward migration toward mid-latitudes, with no significant modification
 429 at low latitudes. For the 14 July 2012 storm (13–18 July), the initial high-latitude depletion progressively extended

430 toward mid-latitudes. During the 17 March 2013 storm (15–20 March), the depletion detected at high latitudes
431 migrated toward Southern Hemisphere mid-latitudes on 18 and 19 March. During the 2 October 2013 storm (2–4
432 October), the O/N₂ reduction initially concentrated at high latitudes propagated toward mid-latitudes on 2 and 3
433 October. Finally, for the 27 February 2014 storm (26 February–3 March), a significant reduction was observed as
434 early as 26 February at southern high latitudes before extending toward mid-latitudes, whereas in the Northern
435 Hemisphere it was detected only on 28 February.

436 **2.4 Discussion**

437 Based on data from a network of GPS receivers distributed in latitude across both hemispheres in the Europe–
438 Africa–Antarctica sector (longitudes 20°E–40°E), and by combining a station-by-station analysis with panel
439 superposition and the use of regional VTEC and Δ VTEC maps, we highlighted contrasting ionospheric responses
440 during geomagnetic storms.

441 The positive, and sometimes negative, variations observed during days classified as magnetically quiet prior to
442 storm onset can be explained by the fact that these days were not entirely free of magnetic disturbances. Thus, for
443 the 17 March 2013 storm, the increase in VTEC recorded on 16 March (reference day) can be attributed to the
444 substorm that occurred around 05 UT, as evidenced by the AE index reaching 863 nT at 04:49 UT. Wei et al. (2009)
445 indeed showed that substorms can induce such increases in VTEC at equatorial latitudes. Previous studies (Kane
446 1973; Araujo-Pradere et al. 2002; Burešová et Laštovička 2007) reported a pre-storm effect on foF2 about 24 h
447 before the SSC, although this interpretation has been debated (Mikhailov et Perrone 2009). Burešová and Laštovička
448 (2007), in a study of 65 major storms between 1995 and 2005, showed that 20–25% of them exhibited a pronounced
449 pre-storm effect.

450 The increase observed prior to the 14 July 2012 storm is consistent with the observations of Tesema et al. (2015),
451 who reported an enhancement of TEC at the equator and northern mid-latitudes, accompanied by a decrease at the
452 EIA crests in both hemispheres. In our case, only the positive effect is remarkable, localized at the transition
453 between low and mid-latitudes. This may be related to the choice of reference, since Tesema et al. (2015) considered
454 only the single quietest day as reference. For the 17 March 2013 storm, Zhu et al. (2022) and Yue et al. (2016)
455 included 16 March in the reference period, which explains the absence of pre-storm anomalies in their results.

456 The persistent negative responses observed at mid and high latitudes during these four storms are mainly explained
457 by a strong depletion of the O/N₂ ratio, as illustrated in Figures 7(a–c). There is indeed a close correlation between
458 electron density and neutral composition variations during storms (Liu et al. 2014). A reduction in atomic oxygen
459 decreases ion production, while an increase in molecular nitrogen enhances ionization losses, leading to a net
460 decrease in electron density (Prölss 1995). Joule heating at high latitudes during storms increases temperature and
461 drives upward winds that transport N₂-rich and O-poor air from the lower thermosphere into the F region
462 (Fuller-Rowell et al. 1994; Qian, Burns, et al. 2014). This process induces a strong horizontal pressure gradient and
463 equatorward neutral winds, causing the O/N₂ deficit to propagate toward mid and low latitudes (Kil et al. 2013;
464 Meier et al. 2015). In parallel, downward motion of O-rich and N₂-poor air at lower latitudes leads to a local
465 increase in the O/N₂ ratio, which can subsequently propagate toward the equator through horizontal transport (Immel
466 et al. 2001; Cai et al. 2022).

467 For the 14 July 2012 storm, the mechanisms responsible for ionospheric asymmetry have been extensively described
468 by Tesema et al. (2015) and Liu et al. (2014). After the SSC (14 July at 18:09 UT), a strong decrease in VTEC
469 appears around 22 UT at stations close to the magnetic equator (NAMA, ADIS, MOIU), while a slight increase is
470 observed at the EIA crests (RAMO, MZUZ). This can be attributed to an equatorward neutral wind, as suggested by
471 the high AE values (1772 nT at 18:48 UT), indicative of significant energy deposition at high latitudes. Such a
472 neutral wind can transport plasma to higher latitudes more efficiently than the super-fountain effect (Liu et al. 2014).
473 The action of an eastward PPEF prior to its reversal westward, followed by redistribution, is also possible. Around
474 19 UT, the interplanetary B_z component oscillated with longer intervals southward than northward and with
475 pressure exceeding 5 nPa, conditions favorable for the generation of a PPEF capable of affecting the E_xB drift.

476 On 15 July, the marked strengthening of the EIA can also be attributed to an eastward PPEF. Before 12 UT, Bz
477 remained southward and the pressure exceeded 20 nPa, again providing favorable conditions for a penetrating
478 electric field. Liu et al. (2014) indeed identified several PPEFs during this event. The decrease observed near the
479 magnetic equator, while other stations showed intensification, confirms this scenario (Liu et al. 2014). The
480 persistence of a pronounced positive phase at northern mid-latitudes around 12 UT may instead be attributed to an
481 enhancement of the equatorial anomaly (Tesema et al. 2015).
482 The contrasting responses recorded between 15 and 16 July are explained by changes in thermospheric composition
483 and the action of storm-induced neutral winds (Tesema et al. 2015; Stankov et al. 2010). Overall, our results confirm
484 previous observations (Akala et al. 2012; Chakraborty et al. 2015; Azzouzi 2016; Tesema et al. 2015), namely a
485 positive TEC response at equatorial low latitudes and a negative response at mid and high latitudes during the 14
486 July 2012 storm.
487 For the 17 March 2013 storm, the inhibition of the EIA, the amplification of the positive response at mid-latitudes,
488 and the observed interhemispheric asymmetry are consistent with the results of Yue et al. (2016), obtained from
489 satellite, ground-based, and theoretical modeling data. These phenomena can be explained by the combined action
490 of polar meridional winds and perturbations of the $E \times B$ drift. Liu et al. (2014) further emphasize that neutral winds
491 play a dominant role in generating vertical ion drifts at mid-latitudes, to the detriment of PPEF effects. The
492 interhemispheric asymmetry may be due to the presence of TADs, as indicated by VTEC oscillations and high AE
493 values (>2500 nT). During equinox periods, electric field and neutral wind effects alone are insufficient to explain
494 this asymmetry, with O/N₂ depletion being more decisive. (Prölss 1995; Zhu et al. 2022; Yue et al. 2016) also
495 showed that TADs can generate such asymmetries in the EIA region during the afternoon. Finally, Migoya-Orué et
496 al. (2021) reported an increase in VTEC over the northern EIA crest in Africa, consistent with our results.
497 During the 2 October storm, the depletion of the O/N₂ ratio (Figure 7c) correlates well with the negative responses
498 observed at high latitudes. However, it is insufficient to explain the persistent disturbances observed at mid-latitudes
499 after the positive phase. These are likely the result of the combined action of O/N₂ depletion and a westward DDEF.
500 The positive disturbances at mid-latitudes and the VTEC oscillations may be related to an eastward PPEF,
501 reinforced by neutral wind action and the presence of TADs. The southward excursion of Bz (-28.8 nT at 04:58 UT)
502 and the strong dynamic pressure (53.17 nPa at 05:25 UT) make the occurrence of a PPEF plausible. Disturbances
503 migrating from high latitudes, associated with high AE values (2089 nT) and VTEC oscillations, are characteristic
504 of TADs (Fuller-Rowell et al. 1994 ; Pandit et al. 2023). The inhibition of the EIA and the amplification of the
505 positive response at mid-latitudes agree with the scenarios proposed by (Yue et al. 2016; Liu et al. 2014). Finally,
506 the difference in the intensity of positive responses between hemispheres can be explained by asymmetric TAD
507 phase velocities related to Joule heating deposition (Zhu et al. 2022).
508 For the 27 February 2014 storm, the high VTEC values recorded prior to onset are consistent with the results of
509 (Malki et al. 2018) at Rabat. Accounting for the time shift, the increase observed around 23 UT on 27 February is
510 also consistent with these studies and is attributed to plasma transport by TADs. The negative responses at high
511 latitudes are correlated with the depletion of the O/N₂ ratio (Figure 7d). The pronounced VTEC increases observed
512 on 1 and 3 March are likely associated with substorms, as suggested by the strong AE enhancements concomitant
513 with decreases in the SYM/H index during these days. Wei et al. (2009) had already shown that such phenomena
514 can increase equatorial VTEC. Finally, the asymmetries observed from the initial phase are consistent with previous
515 observations reporting positive responses in the winter hemisphere and negative responses in the summer
516 hemisphere (Fuller-Rowell et al. 1994).
517 (Shimeis et al. 2015) analyzed TEC variations along a latitudinal chain of GPS stations between 20°E and 40°E,
518 spanning from northern high latitudes to southern high latitudes. Their study revealed strong interhemispheric
519 asymmetry as well as a TID propagating from high to low latitudes. The authors explained that this asymmetry,
520 observed at equinox, results from several concurrent mechanisms, including solar activity, atmospheric dynamo
521 effects, and the offset between geographic and geomagnetic axes.

522 4. Conclusions

523 In this article, we presented an analysis of the ionospheric response during four major geomagnetic storms that
524 occurred between 2012 and 2014, based on data from several GNSS receivers located at low, mid, and high latitudes
525 along a longitude axis between 20° and 40° East.

526 The results show, first of all, that high and mid-latitudes are dominated by persistent negative deviations. These can
527 be explained largely by changes in thermospheric composition during storms, in particular the decrease in the O/N₂
528 ratio, which significantly reduces electron density and contributes directly to the decrease in VTEC. At mid-
529 latitudes, the ionospheric response is more nuanced, marked by alternating positive and negative effects. This
530 variability reflects the combined action of the electric penetration field and neutral circulation. At low latitudes, the
531 dynamics of the equatorial ionospheric anomaly (EIA) showed notable changes, with an intensification during
532 phases dominated by the PPEF, and a suppression under the effect of disturbed neutral winds.

533 Finally, a marked interhemispheric asymmetry was observed, confirming the influence of ionospheric seasonality
534 and TADs on the differential evolution of VTEC between the two hemispheres during a magnetic storm.

535 **Conflict of interest**

536 The authors have declared no conflicts of interest.

537 **Acknowledgements**

538 The authors would like to thank the institutions and services that provided the data used in this study. The RINEX
539 data files from the various stations were obtained from the UNAVCO website (<http://www.unavco.org>). The time
540 series data for solar wind and interplanetary magnetic field parameters (Vsw, Psw, Bz), as well as the AE and
541 SYM/H geomagnetic indices, with a resolution of one minute, were obtained from the OMNI database
542 (https://omniweb.gsfc.nasa.gov/form/omni_min.html). The Kp and Dst indices, as well as the dates of sudden storm
543 commencements (SSCs), are available via the ISGI service (https://isgi.unistra.fr/data_download.php). Finally, the
544 [O/N₂] ratio maps, derived from the Global Ultraviolet Imager (GUVI) aboard the TIMED satellite, were used to
545 interpret the results and are available via the portal https://guvitimed.jhuapl.edu/guvi-gallery13on2_new/.

546 **References**

547 Akala, A. O., P. H. Doherty, C. S. Carrano, C. E. Valladares, et K. M. Groves. 2012. « Impacts of ionospheric
548 scintillations on GPS receivers intended for equatorial aviation applications ». *Radio Science* 47 (04): 1-11.

549 Akala, A.O., A.B. Rabiu, E.O. Somoye, E.O. Oyeyemi, et A.B. Adeloye. 2013. « The Response of African
550 Equatorial GPS-TEC to Intense Geomagnetic Storms during the Ascending Phase of Solar Cycle 24 ». *Journal of
551 Atmospheric and Solar-Terrestrial Physics* 98 (juin): 50-62. <https://doi.org/10.1016/j.jastp.2013.02.006>.

552 Alenazi, Moqbil Salem, Hassan Mahdy Noorelddeen, Ayman Mahmoud Ahmed, et al. 2025. « Investigation of
553 Ionospheric Response to a Moderate Geomagnetic Storm over the Mid-Latitude of Saudi Arabia ». *Open Astronomy*
554 34 (1): 20240009. <https://doi.org/10.1515/astro-2024-0009>.

555 Araujo-Pradere, E. A., T. J. Fuller-Rowell, et M. V. Codrescu. 2002. « STORM: An empirical storm-time
556 ionospheric correction model: 1. Model description ». *Radio Science* 37 (5): 1-12.

557 Astafyeva, E. 2009. « Effects of Strong IMF B_Z Southward Events on the Equatorial and Mid-Latitude Ionosphere ». *Annales Geophysicae* 27 (3): 1175-87. <https://doi.org/10.5194/angeo-27-1175-2009>.

558 Atıcı, Ramazan, et SelçukSağır. 2020. « Global Investigation of the Ionospheric Irregularities during the Severe
559 Geomagnetic Storm on September 7–8, 2017 ». *Geodesy and Geodynamics* 11 (3): 211-21.
560 <https://doi.org/10.1016/j.geog.2019.05.004>.

561 Azzouzi, Ilyasse. 2016. « Impact des évènements solaires sur l'ionisation de l'ionosphère des moyennes et basses
562 latitudes dans le secteur Europe-Afrique ». Université Pierre et Marie Curie- Paris VI; PhD Thesis, Université
563 Mohammed V.

564 Balan, N., K. Shiokawa, Y. Otsuka, et al. 2010. « A physical mechanism of positive ionospheric storms at low
565 latitudes and midlatitudes ». *Journal of Geophysical Research: Space Physics* 115 (A2).

566 Bazié, Nongobsom, Christian Zoundi, M'BI Kaboré, Alfred Jean Stéphane Dama, et Frédéric Ouattara. 2025.
567 « Response of the magnetospheric convection electric field (MCEF) to geomagnetic storms during the solar cycle 24
568 declining phase ». *Journal of the Nigerian Society of Physical Sciences*, 2696-2696.

570 Berényi, K. A., B. Heilig, J. Urbář, D. Kouba, Á. Kis, et V. Barta. 2023. « Comprehensive Analysis of the
 571 Ionospheric Response to the Largest Geomagnetic Storms from Solar Cycle 24 over Europe ». *Frontiers in*
 572 *Astronomy and Space Sciences* 10 (avril): 1092850. <https://doi.org/10.3389/fspas.2023.1092850>.

573 Blanch, E., S. Marsal, A. Segarra, J. M. Torta, D. Altadill, et J. J. Curto. 2013. « Space Weather Effects on Earth's
 574 Environment Associated to the 24–25 October 2011 Geomagnetic Storm ». *Space Weather* 11 (4): 153-68.
 575 <https://doi.org/10.1002/swe.20035>.

576 Buonsanto, M. Ji. 1999. « Ionospheric storms—a review ». *Space Science Reviews* 88 (3): 563-601.

577 Burešová, D., et J. Lašovička. 2007. « Pre-storm enhancements of foF2 above Europe ». *Advances in Space*
 578 *Research* 39 (8): 1298-303.

579 Cai, Xuguang, Wenbin Wang, Alan Burns, Liying Qian, et Richard W. Eastes. 2022. « The Effects of IMF B_y on the
 580 Middle Thermosphere During a Geomagnetically “Quiet” Period at Solar Minimum ». *Journal of Geophysical*
 581 *Research: Space Physics* 127 (5): e2021JA029816. <https://doi.org/10.1029/2021JA029816>.

582 Chakraborty, Monti, Sanjay Kumar, Barin Kumar De, et Anirban Guha. 2015. « Effects of Geomagnetic Storm on
 583 Low Latitude Ionospheric Total Electron Content: A Case Study from Indian Sector ». *Journal of Earth System*
 584 *Science* 124 (5): 1115-26. <https://doi.org/10.1007/s12040-015-0588-3>.

585 Curto, J. J., S. Marsal, E. Blanch, et D. Altadill. 2018. « Analysis of the Solar Flare Effects of 6 September 2017 in
 586 the Ionosphere and in the Earth's Magnetic Field Using Spherical Elementary Current Systems ». *Space Weather* 16
 587 (11): 1709-20. <https://doi.org/10.1029/2018SW001927>.

588 Davies, Kenneth. 1990. *Ionospheric radio*. n° 31. Iet.

589 Fuller-Rowell, T. J., M. V. Codrescu, R. J. Moffett, et S. Quegan. 1994. « Response of the Thermosphere and
 590 Ionosphere to Geomagnetic Storms ». *Journal of Geophysical Research: Space Physics* 99 (A3): 3893-914.
 591 <https://doi.org/10.1029/93JA02015>.

592 Fuller-Rowell, Tim, Mihail Codrescu, Naomi Maruyama, et al. 2007. « Observed and modeled thermosphere and
 593 ionosphere response to superstorms ». *Radio science* 42 (04): 1-9.

594 Gao, Jay. 2008. *Digital analysis of remotely sensed imagery*. McGraw-Hill Professional.

595 Gonzalez, W. D., Jo-Ann Joselyn, Yohsuke Kamide, et al. 1994. « What is a geomagnetic storm? » *Journal of*
 596 *Geophysical Research: Space Physics* 99 (A4): 5771-92.

597 Habyarimana, Valence. 2023. *Jean Bosco Habarulema2 et Teshome Dugassa3*.

598 Hunsucker, Robert D., et John Keith Hargreaves. 2007. *The high-latitude ionosphere and its effects on radio*
 599 *propagation*. Cambridge University Press.

600 Immel, T. J., et A. J. Mannucci. 2013. « Ionospheric redistribution during geomagnetic storms ». *Journal of*
 601 *Geophysical Research: Space Physics* 118 (12): 7928-39.

602 Immel, Thomas J., Geoff Crowley, John D. Craven, et Raymond G. Roble. 2001. « Dayside enhancements of
 603 thermospheric O/N₂ following magnetic storm onset ». *Journal of Geophysical Research: Space Physics* 106 (A8):
 604 15471-88.

605 Kane, R. P. 1973. « Global evolution of F2-region storms ». *Journal of Atmospheric and Terrestrial Physics* 35
 606 (11): 1953-66.

607 Kelley, Michael C. 2009. *The Earth's ionosphere: Plasma physics and electrodynamics*. Vol. 96. Academic press.

608 Kil, H., W. K. Lee, J. Shim, L. J. Paxton, et Y. Zhang. 2013. « The Effect of the 135.6 Nm Emission Originated
 609 from the Ionosphere on the TIMED/GUVI O/N₂ Ratio ». *Journal of Geophysical Research: Space Physics* 118 (2):
 610 859-65. <https://doi.org/10.1029/2012JA018112>.

611 Kuai, Jiawei, Libo Liu, Jing Liu, et al. 2016. « Effects of Disturbed Electric Fields in the Low-latitude and
 612 Equatorial Ionosphere during the 2015 St. Patrick's Day Storm ». *Journal of Geophysical Research: Space Physics*
 613 121 (9): 9111-26. <https://doi.org/10.1002/2016JA022832>.

614 Liu, Jing, Libo Liu, Takuji Nakamura, Binqiang Zhao, Baiqi Ning, et A. Yoshikawa. 2014. « A Case Study of
 615 Ionospheric Storm Effects during Long-lasting Southward IMF B_z -driven Geomagnetic Storm ». *Journal of*
 616 *Geophysical Research: Space Physics* 119 (9): 7716-31. <https://doi.org/10.1002/2014JA020273>.

617 Liu, Yi Y., Richard AM De Jeu, Matthew F. McCabe, Jason P. Evans, et Albert IJM Van Dijk. 2011. « Global
 618 long-term passive microwave satellite-based retrievals of vegetation optical depth ». *Geophysical Research Letters*
 619 38 (18).

620 Malki, Khalifa, Aziza Bounhir, Zouhair Benkhaldoun, et al. 2018. « Ionospheric and Thermospheric Response to the
 621 27–28 February 2014 Geomagnetic Storm over North Africa ». *Annales Geophysicae* 36 (4): 987-98.
 622 <https://doi.org/10.5194/angeo-36-987-2018>.

623 Mao, Tian, Lingfeng Sun, Lianhuan Hu, Yungang Wang, et Zhijun Wang. 2015. « A Case Study of Ionospheric
 624 Storm Effects in the Chinese Sector during the October 2013 Geomagnetic Storm ». *Advances in Space Research* 56
 625 (9): 2030-39. <https://doi.org/10.1016/j.asr.2015.05.045>.

626 Matamba, Tshimangadzo Merline, John Bosco Habarulema, et Lee-Anne McKinnell. 2015. « Statistical analysis of
 627 the ionospheric response during geomagnetic storm conditions over South Africa using ionosonde and GPS data ».
 628 *Space Weather* 13 (9): 536-47.

629 Meier, R. R., J. M. Picone, D. Drob, et al. 2015. « Remote Sensing of Earth's Limb by TIMED/GUVI: Retrieval of
 630 Thermospheric Composition and Temperature ». *Earth and Space Science* 2 (1): 1-37.
 631 <https://doi.org/10.1002/2014EA000035>.

632 Mendillo, M., et C. Narvaez. 2009. « Ionospheric storms at geophysically-equivalent sites—Part 1: Storm-time
 633 patterns for sub-auroral ionospheres ». *Annales Geophysicae* 27 (4): 1679-94.

634 Mendillo, M., et C. Narvaez. 2010. « Ionospheric storms at geophysically-equivalent sites—Part 2: Local time storm
 635 patterns for sub-auroral ionospheres ». *Annales Geophysicae* 28 (7): 1449-62.

636 Mendillo, Michael. 2006. « Storms in the ionosphere: Patterns and processes for total electron content ». *Reviews of
 637 Geophysics* 44 (4).

638 Migoya-Orué, Y. O., S. M. Radicella, et P. Coïsson. 2009. « Low latitude ionospheric effects of major geomagnetic
 639 storms observed using TOPEX TEC data ». *Annales geophysicae* 27 (8): 3133-39.

640 Migoya-Orué, Yenca, Katy Alazo-Cuertas, Anton Kashcheyev, et al. 2021. « B2 Thickness Parameter Response to
 641 Equinoctial Geomagnetic Storms ». *Sensors* 21 (21): 7369. <https://doi.org/10.3390/s21217369>.

642 Mikhailov, A. V. et L. Perrone. 2009. « Pre-storm NmF2 enhancements at middle latitudes: delusion or reality ? »
 643 *Annales Geophysicae* 27 (3): 1321-30.

644 Omojola, Joseph, et Taiwo Adewumi. 2019. « Effects of St Patrick's Day Intervals Geomagnetic Storms on the
 645 Accuracy of GNSS Positioning and Total Electron Content over Nigeria ». <https://doi.org/10.22059/jesphys.2019.259772.1007014>, n° Online
 646 First (janvier). <https://doi.org/10.22059/jesphys.2019.259772.1007014>.

647 Ouattara, Frédéric, Christian Zoundi, Christine Amory MAZAUDIER, Rolland FLEURY, et Patrick LASSUDRIE
 648 DUCHESNE. 2011. « Détermination du contenu électronique total à partir des pseudo distances (Pd) ou pseudo
 649 range (Pr) a la station de Koudougou au Burkina Faso ». *Journal des Sciences* 11: 12-19.

650 Ouédraogo, Pouraogo, Karim Guibula, Abidina Diabaté, Rolland Fleury, et Frédéric Ouattara. 2024. « Study of
 651 Regular Variations in Vertical Total Electron Content (VTEC) from 2013 to 2021 at Station BF01 in
 652 Ouagadougou ». *Current Journal of Applied Science and Technology* 43 (7): 103-17.
 653 <https://doi.org/10.9734/cjast/2024/v43i74410>.

654 Pandit, D., C. Amory-Mazaudier, R. Fleury, N. P. Chapagain, et B. Adhikari. 2023. « VTEC Observations of Intense
 655 Geomagnetic Storms above Nepal: Comparison with Satellite Data, CODE and IGSG Models ». *Indian Journal of
 656 Physics* 97 (3): 701-18. <https://doi.org/10.1007/s12648-022-02441-w>.

657 Pedatella, Nicholas M., Jiahou Lei, Kristine M. Larson, et Jeffrey M. Forbes. 2009. « Observations of the
 658 ionospheric response to the 15 December 2006 geomagnetic storm: Long-duration positive storm effect ». *Journal
 659 of Geophysical Research: Space Physics* 114 (A12).

660 Prölss, G. W. 1995. *Handbook of Atmospheric Electrodynamics, Volume II*Handbook of Atmospheric. CRC Press.

661 Pulkkinen, Tuija. 2007. « Space Weather: Terrestrial Perspective ». *Living Reviews in Solar Physics* 4.
 662 <https://doi.org/10.12942/lrsp-2007-1>.

663 Qian, Liying, Alan G Burns, Barbara A Emery, et al. 2014. « The NCAR TIE-GCM: A community model of the
 664 coupled thermosphere/ionosphere system ». *Modeling the ionosphere–thermosphere system*, 73-83.

665 Qian, Liying, Stanley C. Solomon, et Raymond G. Roble. 2014. « Secular changes in the thermosphere and
 666 ionosphere between two quiet Sun periods ». *Journal of Geophysical Research: Space Physics* 119 (3): 2255-62.
 667 Richmond, A. D., et G. Lu. 2000. « Upper-atmospheric effects of magnetic storms: a brief tutorial ». *Journal of
 668 Atmospheric and Solar-Terrestrial Physics* 62 (12): 1115-27.
 669 Rishbeth, H., et I. C. F. Müller-Wodarg. 2006. « Why is there more ionosphere in January than in July? The annual
 670 asymmetry in the F2-layer ». *Annales Geophysicae* 24 (12): 3293-311.
 671 Sawadogo, Saguedo, Doua Allain Gnabahou, Sibri Alphonse Sandwidi, et Frédéric Ouattara. 2023. « Koudougou
 672 (Burkina Faso, Africa), GPS-TEC Response to Recurrent Geomagnetic Storms during Solar Cycle 24 Declining
 673 Phase ». *International Journal of Geophysics* 2023 (avril): 1-13. <https://doi.org/10.1155/2023/4181389>.
 674 Sharma, Sunil Kumar, Arun Kumar Singh, Sampad Kumar Panda, et Sameh S. Ahmed. 2020. « The Effect of
 675 Geomagnetic Storms on the Total Electron Content over the Low Latitude Saudi Arab Region: A Focus on St.
 676 Patrick's Day Storm ». *Astrophysics and Space Science* 365 (2): 35. <https://doi.org/10.1007/s10509-020-3747-1>.
 677 Shimeis, A., C. Borries, C. Amory-Mazaudier, et al. 2015. « TEC Variations along an East Euro-African Chain
 678 during 5th April 2010 Geomagnetic Storm ». *Advances in Space Research* 55 (9): 2239-47.
 679 <https://doi.org/10.1016/j.asr.2015.01.005>.
 680 Shreedevi, P. R., et R. K. Choudhary. 2017. « Impact of Oscillating IMF B_z During 17 March 2013 Storm on the
 681 Distribution of Plasma Over Indian Low-Latitude and Mid-Latitude Ionospheric Regions ». *Journal of Geophysical
 682 Research: Space Physics* 122 (11). <https://doi.org/10.1002/2017JA023980>.
 683 Silwal, Ashok, Sujan Prasad Gautam, Prakash Poudel, Monika Karki, Narayan P Chapagain, et Binod Adhikari.
 684 2023. « Variation of Total Electron Content over Nepal during Geomagnetic Storms: GPS Observations ». *Russian
 685 Journal of Earth Sciences*, août 13, 1-19. <https://doi.org/10.2205/2023ES000833>.
 686 Stankov, S. M., Koen Stegen, et René Warnant. 2010. « Seasonal variations of storm-time TEC at European middle
 687 latitudes ». *Advances in Space Research* 46 (10): 1318-25.
 688 Tesema, F., B. Damtie, et M. Nigussie. 2015. « The Response of the Ionosphere to Intense Geomagnetic Storms in
 689 2012 Using GPS-TEC Data from East Africa Longitudinal Sector ». *Journal of Atmospheric and Solar-Terrestrial
 690 Physics* 135 (décembre) : 143-51. <https://doi.org/10.1016/j.jastp.2015.10.021>.
 691 Tsurutani, Bruce T., Walter D. Gonzalez, et Yohsuke Kamide. 1997. « Magnetic storms ». *Surveys in geophysics* 18
 692 (4): 363-83.
 693 Uga, Chali Idosa, Sujan Prasad Gautam, et Ephrem Beshir Seba. 2024. « TEC Disturbances Caused by CME-
 694 Triggered Geomagnetic Storm of September 6–9, 2017 ». *Heliyon* 10 (10): e30725.
 695 <https://doi.org/10.1016/j.heliyon.2024.e30725>.
 696 Vijaya Lekshmi, D., N. Balan, S. Tulasi Ram, et J. Y. Liu. 2011. « Statistics of Geomagnetic Storms and
 697 Ionospheric Storms at Low and Mid Latitudes in Two Solar Cycles : GEOMAGNETIC AND IONOSPHERIC
 698 STORMS ». *Journal of Geophysical Research: Space Physics* 116 (A11): n/a-n/a.
 699 <https://doi.org/10.1029/2011JA017042>.
 700 Wei, Y., Z. Pu, M. Hong, et al. 2009. « Westward ionospheric electric field perturbations on the dayside associated
 701 with substorm processes ». *Journal of Geophysical Research: Space Physics* 114 (A12).
 702 Yu, Tingting, Wenbin Wang, Zhipeng Ren, Xuguang Cai, et Maosheng He. 2023. « Vertical Variations in
 703 Thermospheric O/N₂ and the Relationship Between O and N₂ Perturbations During a Geomagnetic Storm ». *Earth
 704 and Space Science* 10 (10): e2023EA002988. <https://doi.org/10.1029/2023EA002988>.
 705 Yue, Xinan, William S. Schreiner, Nicholas Pedatella, et al. 2014. « Space weather observations by GNSS radio
 706 occultation : From FORMOSAT-3/COSMIC to FORMOSAT-7/COSMIC-2 ». *Space Weather* 12 (11): 616-21.
 707 Yue, Xinan, Wenbin Wang, Jiuhou Lei, et al. 2016. « Long-lasting Negative Ionospheric Storm Effects in Low and
 708 Middle Latitudes during the Recovery Phase of the 17 March 2013 Geomagnetic Storm ». *Journal of Geophysical
 709 Research: Space Physics* 121 (9): 9234-49. <https://doi.org/10.1002/2016JA022984>.
 710 Zhu, Qingyu, Gang Lu, et Yue Deng. 2022. « Low- and Mid-Latitude Ionospheric Response to the 2013 St.
 711 Patrick's Day Geomagnetic Storm in the American Sector: Global Ionosphere Thermosphere Model Simulation ».
 712 *Frontiers in Astronomy and Space Sciences* 9 (mai): 916739. <https://doi.org/10.3389/fspas.2022.916739>.

713 Zoundi, c., et f. Ouattara. S. D. *Processus de détermination du contenu électronique total (cet) process for*
714 *determining total electron content (TEC).*

715

716

UNDER PEER REVIEW N IJAR